Spontaneous Generation of Near-Inertial Waves by the Kuroshio Front

Takeyoshi Nagai

Tokyo University of Marine Science and Technology, Tokyo, Japan

Amit Tandon

University of Massachusetts Dartmouth, North Dartmouth, Massachusetts

Eric Kunze

NorthWest Research Associates, Redmond, Washington

Amala Mahadevan

Woods Hole Oceanographic Institution, Woods Hole, Massachusetts

ABSTRACT

While near-inertial waves are known to be generated by atmospheric storms, recent observations in the Kuroshio Front find intense near-inertial internal-wave shear along sloping isopycnals, even during calm weather. Recent literature suggests that spontaneous generation of near-inertial waves by frontal instabilities could represent a major sink for the subinertial quasigeostrophic circulation. An unforced three-dimensional 1-km-resolution model, initialized with the observed cross-Kuroshio structure, is used to explore this mechanism. After several weeks, the model exhibits growth of 10–100-km-scale frontal meanders, accompanied by $O(10)$ mW m^{-2} spontaneous generation of near-inertial waves associated with readjustment of submesoscale fronts forced out of balance by mesoscale confluent flows. These waves have properties resembling those in the observations. However, they are reabsorbed into the model Kuroshio Front with no more than 15% dissipating or radiating away. Thus, spontaneous generation of near-inertial waves represents a redistribution of quasigeostrophic energy rather than a significant sink.

1. Introduction

Most of the power into the ocean's general circulation arises from stress exerted by the wind at the surface (Fofonoff 1981; Oort et al. 1994; Wunsch 1998). Because of the ocean's boundaries, wind patterns, density distribution, and Earth's rotation, this energy organizes into 100–1000-km gyres and currents and fields of 10–100-km mesoscale eddies. This large-scale quasigeostrophic dynamics arrests transfer of energy to smaller scales where it could be dissipated, instead cascading energy to larger scales. But energy in the general circulation must be dissipated at the same 1-TW rate that it is forced by wind.

Several dissipation mechanisms have been proposed involving interactions with bottom or lateral boundaries (Fig. 1) including 0.2 TW in internal lee-wave generation (Nikurashin and Ferrari 2011) and 0.1 TW of bottom drag (Wunsch and Ferrari 2004). However, these forces are negligible away from boundaries (Wunsch and Ferrari 2004) and fall short of the power input. Hence, there remains a gap in our understanding of how the interior ocean subinertial circulation dissipates.

Several studies have pointed out that fronts can spontaneously generate inertia–gravity waves. Using a two-dimensional numerical model, Snyder et al. (1993) showed that atmospheric fronts forced out of balance by frontogenetic confluence can spontaneously radiate inertia–gravity waves as they undergo geostrophic adjustment (Rossby 1938). Plougonven and Snyder (2007) found that near-inertial waves are radiated from a meandering atmospheric front and stall near the front. Ford (1994)

Corresponding author address: Takeyoshi Nagai, Japan Tokyo University of Marine Science and Technology, 4-5-7 Konan, Minatoku, Tokyo 108-8477, Japan.
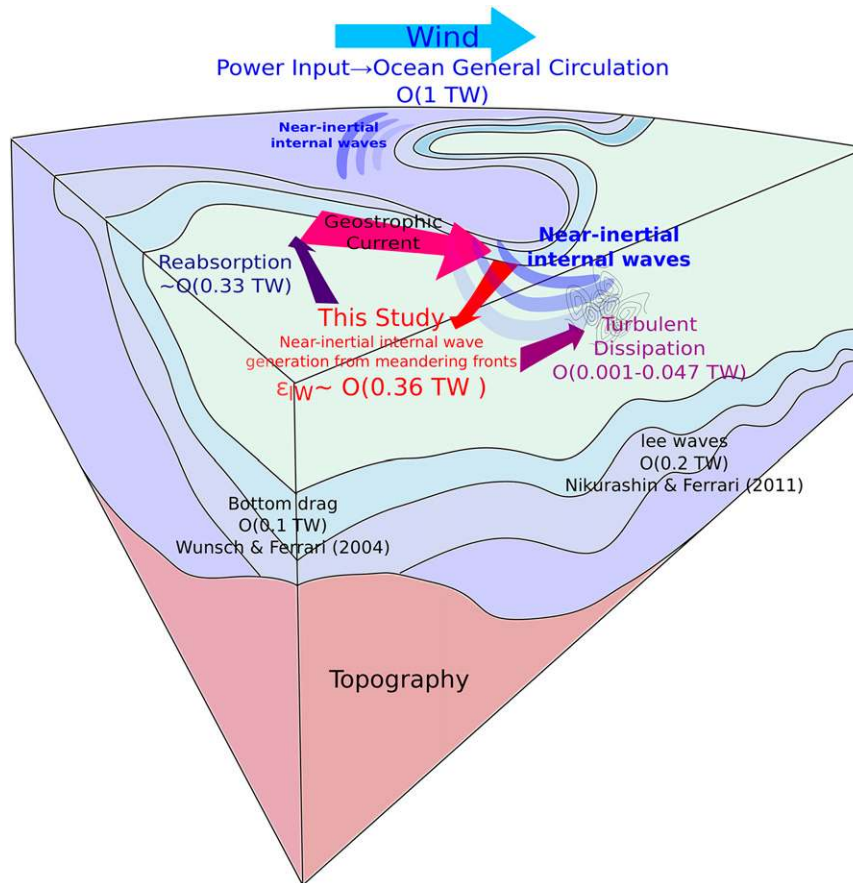E-mail: tnagai@kaiyodai.ac.jp

FIG. 1. Schematic of this study. Wind power input to the ocean general circulation is estimated to be $O(1)$ TW (Wunsch 1998). This power input is balanced by energy dissipation processes such as bottom drag $O(0.1)$ TW (Wunsch and Ferrari 2004) and lee-wave generation $O(0.2$ TW) (Nikurashin and Ferrari 2011) near the bottom boundary. The study described here suggests that an unforced front can lose power from balanced circulations to near-inertial waves of $O(0.36)$ TW. However, most of this is reabsorbed into the balanced flows with relatively little lost to explicit model dissipation $O(0.001–0.047)$ TW.

showed that barotropic shallow-water models with zonal bands of anomalous PV radiate inertia–gravity waves from evolving vortices. Similarly, Danioux et al. (2012) used a 2-km-resolution primitive equation ocean model to show that gravity waves are emitted from high-Rossby-number flow associated with density filaments near the surface. Shakespeare and Taylor (2014) showed analytically that a two-dimensional front undergoing frontogenesis can radiate inertia–gravity waves that remain trapped and amplified within the front by the confluent flow. In laboratory experiments, Williams et al. (2008) found that the amplitude of the emitted waves from balanced flow is linearly proportional to Rossby number, estimating that 1.5 TW could be transferred from the balanced flow to internal gravity waves in the ocean. Based on estimates of the mesoscale eddy/internal-wave momentum transfer coefficients in the Sargasso Sea (Polzin 2010), Ferrari and

Wunsch (2009) inferred a global net transfer rate of 0.35 TW. From an analytic model for minimum-frequency near-inertial waves in a baroclinic front under the influence of confluent flow, Thomas (2012) suggested a 0.1-TW global loss of balanced energy to near-inertial waves.

Based on the order-of-magnitude spread in the above estimates, the energy that can be drained from the sub-inertial quasigeostrophic flows of the ocean general circulation by spontaneous generation of internal waves remains uncertain. Here, we explore this possible sink for quasigeostrophic energy numerically. We motivate this study with numerous recent measurements that show enhanced near-inertial shear in the Kuroshio Front and Gulf Stream (section 2). Unforced numerical simulations of the Kuroshio spontaneously generate near-inertial waves to reproduce the observed near-inertial shear and enhancement of turbulent dissipation under the

front (section 3). Global internal-wave power gain, through spontaneous radiation from fronts forced out of balance by confluent flows followed by reabsorption and dissipation, is estimated in section 4, and conclusions are summarized in section 5.

2. Observations of near-inertial waves in the Kuroshio

a. Kuroshio surveys

To motivate our study, we first describe four transect surveys. Three transects were sampled across the Kuroshio Front along 143°E during 8–10 August 2008 and 8–10 August 2011 and along 142°E during 9–11 August 2012. In these field programs, expendable bathythermographs (XBT T-7s) were deployed every 3.7 km in 2008 and 2011 and 2.8 km in 2012 to measure temperature in the upper 750 m from 36°36′ to 35°N during 2008, 36°30′ to 34°30′N during 2011, and 35°44′ to 34°19′N during 2012. A freefall towyo CTD (Underway CTD) was used to measure upper-500-m temperature and salinity every 14.8 km in the 2012 survey. During 2008, five Falmouth CTD profiles of temperature and salinity to 500-m and TurboMAP-II microstructure profiles to 300-m depth were collected every 28 km (Nagai et al. 2009). During 17–24 October 2009, five north–south transects were sampled across the Kuroshio to measure CTD and microstructure at 5–8 stations with 9-km resolution in each section (Nagai et al. 2012). During 2011 and 2012, five CTD and four TurboMAP-L (Doubell et al. 2009) profiles were collected every 9.3 km and expendable CTDs (XCTD) were dropped at the north and south ends of the transect.

To obtain salinity with the same resolution as XBT temperature, an optimal interpolation was performed for the CTD data with monthly salinity climatology from the *World Ocean Atlas 2005* using 20 km and 40 m as horizontal and vertical decorrelation scales. Buoyancy is defined as $b = -g(\rho - \rho_o)\rho_o^{-1}$, where ρ is the potential density calculated from temperature and salinity using the equation of state of seawater (EOS-80), the reference density $\rho_o = 1025$ kg m^{-3}, and g is the gravitational acceleration. Turbulent kinetic energy dissipation rates are computed by integrating microscale shear spectra over the wavenumber band where they agree with the Nasmyth (1970) model spectrum—that is, from approximately 1 m down to twice the Kolmogorov scale.

Currents were measured using a 38.4-kHz Teledyne RD ADCP (30° beam angle, 3.6° beamwidth) and 130-kHz Furuno ADCP. During 2008, the Teledyne measured flows to 1218-m depth in 16-m bins with 16-m transmitted pulse length while, during 2011, it measured to 1018-m
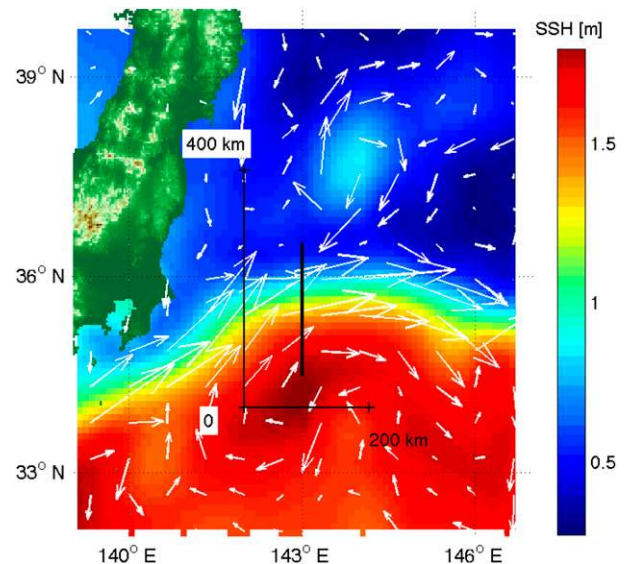

FIG. 2. Satellite sea surface height (absolute dynamic topography) (color) of the Kuroshio Front east of Japan around 8 Aug 2011 superimposed with (i) geostrophic currents inferred from absolute dynamic topography (white arrows), (ii) the ship track (meridional thick black line), and (iii) the horizontal dimensions of the numerical domain in Fig. 5 (thin black lines). Topography of Honshu Island is shown in green shading.

depth in 10-m bins with 11.59-m transmitted pulse length. The vertical wavenumber spectra for zonal ADCP shear $u_z(z)$ near the Kuroshio Front suggest signal attenuation around 30-m vertical wavelength (not shown) so that vertical shear on larger wavelengths is resolved.

During August 2011, the Kuroshio flowed along a relatively stable path with a strong eastward flow exceeding 2 m s^{-1} at the observational line (Fig. 2). The high-pressure warm-core eddy north of the Kuroshio (Fig. 2) provided confluent flow near the observation sites. During 2008, the Kuroshio was relatively unstable, exhibiting 100-km-scale meanders upstream of the transect (Fig. 1 of Nagai et al. 2009).

b. Near-inertial shear

To isolate the spatial structure of near-inertial shear across the Kuroshio Front, residual shear is extracted by subtracting alongfront geostrophic shear $fu_z^g = -b_y$ from ADCP-measured shear u_z—that is, $u_z^a = u_z - u_z^g = u_z + b_y/f$, where y is the cross-front coordinate, b_y is based on our cross-front density measurements, and subscripts denote derivatives. Before subtraction, buoyancy and velocity data are smoothed and linearly interpolated of grid with a 3.7-km horizontal and 1-m vertical resolution. Because our transect is nearly normal to the Kuroshio, the ADCP-measured meridional shear v_z is assumed to have no geostrophic contribution
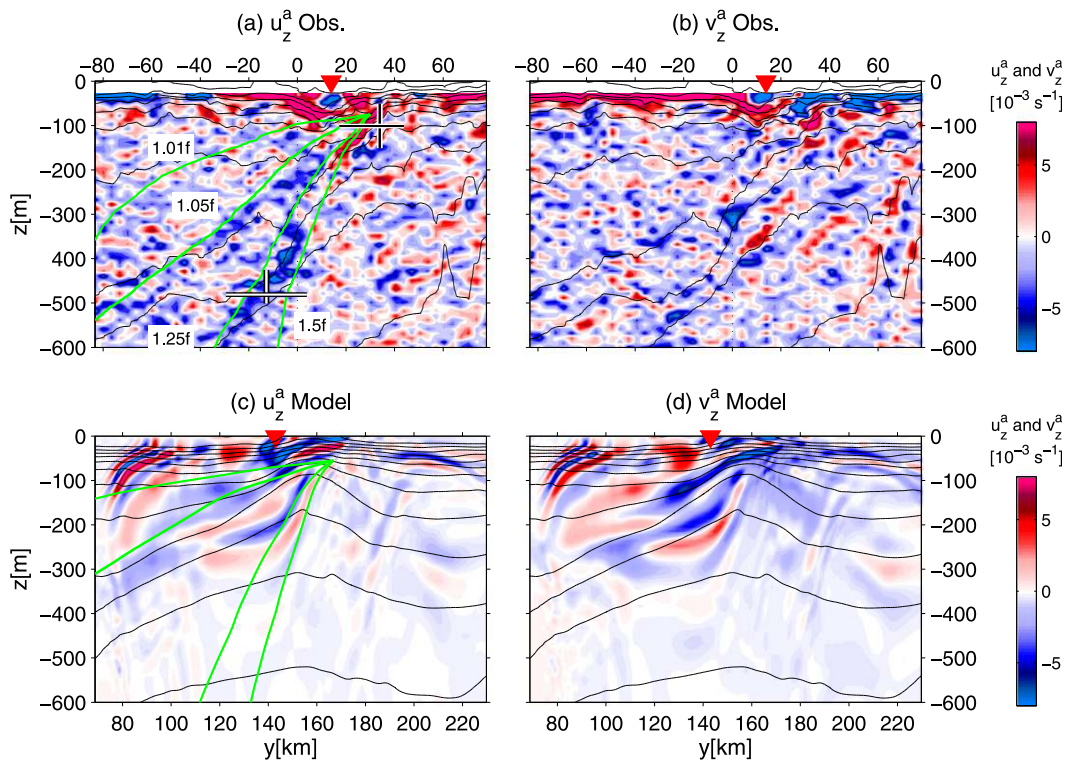
FIG. 3. Meridional sections of (a) back-rotated observed zonal residual vertical shear $u_z^a = u_z + b_y f^{-1}$, (b) meridional residual vertical shear $v_z^a = v_z$, and model (c) $u_z^a = u_z + b_y f^{-1}$ and (d) $v_z^a = v_z - b_x f^{-1}$ at $x = 100$ km and at day 11.25. As our observational transect was nearly normal to the Kuroshio flow, measured meridional shear is considered to be residual vertical shear $v_z^a = v_z$. Black lines are isopycnals every 0.5 kg m^{-3}, showing that the model front is shallower and gentler than the measured front in these snapshots but inertial shear banding has comparable slopes to isopycnals in the upper-ocean fronts in both. Green curves in (a) and (c) denote near-inertial ray paths under quiescent conditions for the labeled frequencies. Red triangles represent position of the front, defined by the maximum value of vertically averaged horizontal buoyancy gradient.

(i.e., $v_z^a = v_z$), consistent with its alternating positive and negative signs (Fig. 3b).

Near-inertial shear rotates clockwise in time. To avoid temporal aliasing of the horizontal structure when observations span an interval (17 h in our case) that exceeds or is similar to the inertial time scale $f^{-1}[=P_f/(2\pi) = 3.5$ h at our location where P_f is the inertial period], back-rotated residual shear $u_z^a(t_0)$ referenced to time t_0 is estimated from the observations $Z(t) = u_z^a(t) + iv_z^a(t)$ at varying times t as

$$Z(t_0) = \text{Re}[Z(t)e^{i(t-t_0)f}]. \quad (1)$$

Back-rotated residual vertical shear $Z(t_0)$ exhibits bandedness in the Kuroshio Front (Fig. 3a) of similar magnitudes as observed during 2008 (Nagai et al. 2009) and previous studies in the Kuroshio (Rainville and Pinkel 2004) and Gulf Stream (Winkel et al. 2002; Inoue et al. 2010). Horizontal and vertical wavelengths are $\lambda_h \sim O(10)$ km and $\lambda_z \sim O(100)$ m, respectively. The internal-wave dispersion relation then implies that the frequency of

these waves $\omega = \sqrt{f^2 + N^2 \lambda_z^2 / \lambda_h^2} \approx f$, based on the estimated $N \sim O(10^{-2})\,\text{s}^{-1}$ and local $f \sim O(10^{-4})\,\text{s}^{-1}$. This is consistent with the assumption that the frequency of the shear bands is near inertial. Hodographs of the residual shear are rotary with depth and meridian as expected for propagating near-inertial internal waves, suggesting energy radiation northward and upward on the north side (Figs. 4b and 4d) and southward and downward on the south side of the Kuroshio Front (Figs. 4a and 4c).

During 2011, a typhoon passed 500 km south of the region two weeks prior to the observations, but the time elapsed since the storm far exceeds the 2–4-day time scale expected for propagation $|\Delta r|/|C_g|$, where r is the distance and C_g the group speed, or dissipation E/ε, where E is the inertial wave energy and ε is the dissipation rate of the waves. The wind during the 2011 cruise was weak with speeds of 5–10 m s^{-1}. Results from a slab model (Pollard and Millard 1970) for mixed-layer inertial motions forced with reanalyzed hourly winds from the week prior to the typhoon (GPV-MSM-S of the Japan Meteorological Agency; Saito et al. 2006)
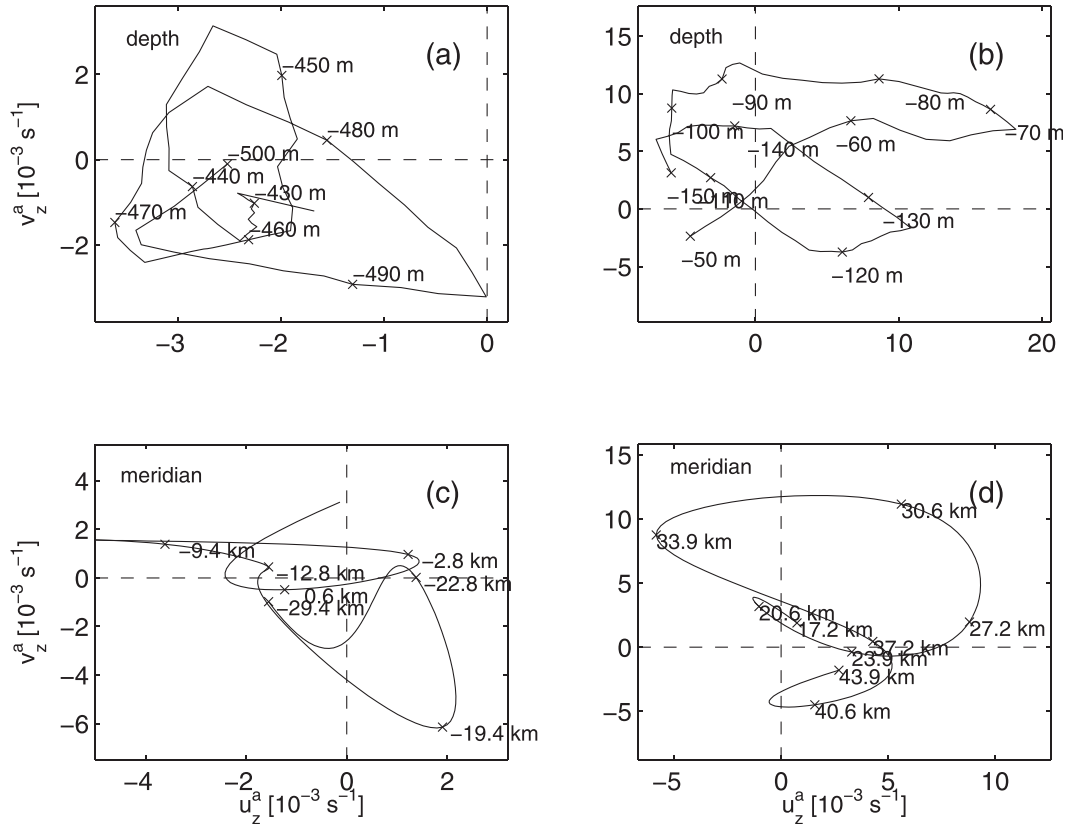
FIG. 4. (a),(b) Depth hodographs of back-rotated ageostrophic shear (10^{-3} s^{-1}) along the (a) black–white–black solid vertical bar in the bottom left and (b) white–black–white vertical bar in the top right of Fig. 3a with depths indicated. (c),(d) Meridional hodographs along the (c) black–white–black and (d) white–black–white horizontal bar in Fig. 3a, with distances from the front indicated. Spline interpolation was used for the residual vertical shear in the meridional hodographs (c),(d).

show weaker cumulative wind power input to inertial motions ($\sim$1000 J m^{-2}) compared to the near-inertial horizontal kinetic energy integrated between 100- and 750-m depth near the Kuroshio Front ($\sim$5000 J m^{-2}; not shown).

In summary, observed bands of near-inertial shear (i) appear to be stronger near the front (Fig. 3a), (ii) recur from year to year as well as being found in other western boundary current fronts (Winkel et al. 2002; Rainville and Pinkel 2004; Inoue et al. 2010), and (iii) appear to be unrelated to surface forcing, though this cannot be established unequivocally with our limited data. Near-inertial waves can be trapped and amplified by frontal shears (Kunze 1985; Whitt and Thomas 2013) and wind-generated waves may stall in fronts long after forcing. While these alternative possibilities cannot be discounted based on available data, here these observations motivate numerical investigation into the hypothesis that the observed near-inertial shear arises from internal dynamics associated with frontogenesis (frontal strengthening) and frontolysis (frontal weakening) of the Kuroshio Front.

3. Model simulation of the Kuroshio Front

a. Model setup

We use the three-dimensional nonhydrostatic equation process study ocean model (PSOM) (Mahadevan et al. 1996a,b) to investigate generation of near-inertial waves by frontal instability. The model horizontal resolution is 1 km and domain dimensions 192 and 384 km in zonal (x) and meridional (y) directions, respectively. There are 64 vertical levels in the model with a flat bottom at 750-m depth. The vertical resolution is a few meters in the upper 150 m and telescopes from $\sim$5 to 30 m between 150- and 750-m depth. Zonal boundaries are periodic while meridional boundaries rigid walls. Sponge layers of 35-km width along the north and south boundaries suppress reflection of propagating waves. The bottommost layer is also a sponge layer. Horizontal diffusivities are 500 m^2 s^{-1} within the sponge layers and 1 m^2 s^{-1} elsewhere. Within the north and south sponge layers, there is additional Rayleigh damping $-\alpha_o\mathbf{u}$ with decay rate $\alpha_o = 2$ days^{-1}

and velocity vector **u**. Based on vertical internal-wave energy fluxes, bottom generation of internal waves was found to be negligible in all of the simulations. Vertical diffusivities are $10^{-5} \, \text{m}^2 \, \text{s}^{-1}$ everywhere. No hyperviscosities or hyperdiffusivities are used.

To provide realistic initial conditions for the modeled Kuroshio, the 2008 grid-averaged meridional density section (Nagai et al. 2009) is used. To suppress initial unbalanced disturbances in the simulation, temperature and salinity at each vertical level across the front are fitted with high-order polynomial functions. Potential densities calculated from temperature and salinity are then sorted to be vertically monotonic so as to remove any gravitationally unstable density inversions; density inversions are present in 3% of the original unsorted 1-m data. The resulting density field is linearly interpolated onto the 1-km horizontal model grid.

To induce a frontal meander, a sinusoidal fluctuation is introduced in the initial condition by shifting the initial vertical section meridionally by $\delta y = A \sin(x \pi / L_x)$, where δy is the meridional displacement, $A = 3 \, \text{km}$ is the displacement amplitude, x is the zonal coordinate, and $L_x = 96 \, \text{km}$ is half the zonal wavelength. The velocity is initialized to be everywhere in geostrophic balance. The initial quasigeostrophic imbalance is quantified by computing the magnitude of the frontogenetic **Q** vector $(|-u_x^g b_x - v_x^g b_y, \ -u_y^g b_x - v_y^g b_y|$; see also section 4a) on the initial state which is found to be only 1% of that after frontal meanders develop fully on day 11.25. Large-amplitude inertial oscillations are not generated at the outset but only arise after the meanders develop fully as described below. The Ertel potential vorticity of the initial condition is confirmed to be everywhere positive. Accordingly, the initial flow field is gravitationally and symmetrically stable.

b. Evolution of the model flow field

As the model solution evolves, baroclinic instability generates a ~100-km-scale meander and eddy on a time scale of weeks. At this $O(\text{weeks})$ time in the simulation, model mesoscale fields (Fig. 5) are similar to those often observed in the Kuroshio Front (e.g., Fig. 1a in Nagai et al. 2009; Kouketsu et al. 2007). The magnitude of the model 30-h average confluence $\sqrt{(u_x - v_y)^2 + (v_x + u_y)^2}$ is comparable to the magnitude of cross-front confluence $|v_y| \sim O(10^{-6} - 10^{-5}) \, \text{s}^{-1} \sim O(0.01f - 0.1f)$ in the upper 300 m near the Kuroshio estimated from a 45-km meridionally smoothed ADCP transect. Within this meandering mesoscale field, vertical shear, vorticity $(v_x - u_y)/f$, and horizontal divergence $(u_x + v_y)/f$ exhibit submesoscale banding (Figs. 5 and 6) within fronts with

similar horizontal wavelengths of $O(10) \, \text{km}$ to those observed—although the particular model front snapshot displayed is shallower and less steep than the observed front (Fig. 3). The banded structures emerge, not in the initial stages of the simulation, but within an inertial period after the development of meanders and mesoscale eddy interaction with the main stream. As established below, these banded structures are near-inertial waves.

To filter out the subinertial flow, Eulerian high-pass quantities are obtained by subtracting 30-h averages from instantaneous data, where 30 h was chosen because the lowest internal-wave frequencies are modulated by geostrophic shears (Kunze 1985; Whitt and Thomas 2013) and Doppler shifting in the Eulerian frame. The high-pass fields include both internal waves and Doppler-shifted subinertial structures; Eulerian 30-h high-pass velocity is strongly correlated with Eulerian high-pass pressure gradient (not shown), suggesting a significant contribution from thermal wind.

Frequencies in an Eulerian frame can be difficult to interpret dynamically owing to Doppler shifting by subinertial front and eddy flows. To characterize the frequencies of the banded structure in a Lagrangian frame, we introduce 10 000 virtual massless particles (drifters) near the center of the model front at 50–150-m depth. These particles are advected passively by the three-dimensional flow without influencing the dynamics. Four Lagrangian particles are selected as examples to record high-pass flow fields for 20 days as they pass through the region of strong banded signals that mostly lie along the main stream (Fig. 7a). The resulting Lagrangian rotary spectra are clockwise in time for frequencies between f and $2f$ (Figs. 8a and 8b), confirming that the banding in the Eulerian high-pass quantities is near-inertial waves. The relatively broad peaks in the spectra are likely caused by modulation of the lowest allowed internal-wave frequency by geostrophic vorticity (Kunze 1985) and baroclinicity (Mooers 1975; Whitt and Thomas 2013).

Hodographs of residual shear $(u_z^a = u_z + b_y/f, \ v_z^a = v_z - b_x/f)$ exhibit signatures of vertically propagating near-inertial waves (Fig. 9), rotating clockwise in time (Figs. 9c and 9e), clockwise with depth over 200–400-m depth on day 10.5 (Fig. 9d), and counterclockwise with depth over 100–200-m depth on day 16 (Fig. 9f). Lack of perfect circularity (Figs. 9c–f) may be a signature of the superinertial nature of the waves, for which the major-to-minor axis ratio should be ω/f, or due to subinertial baroclinicity that rectifies cross-front waves with phase lines parallel to steeply sloping
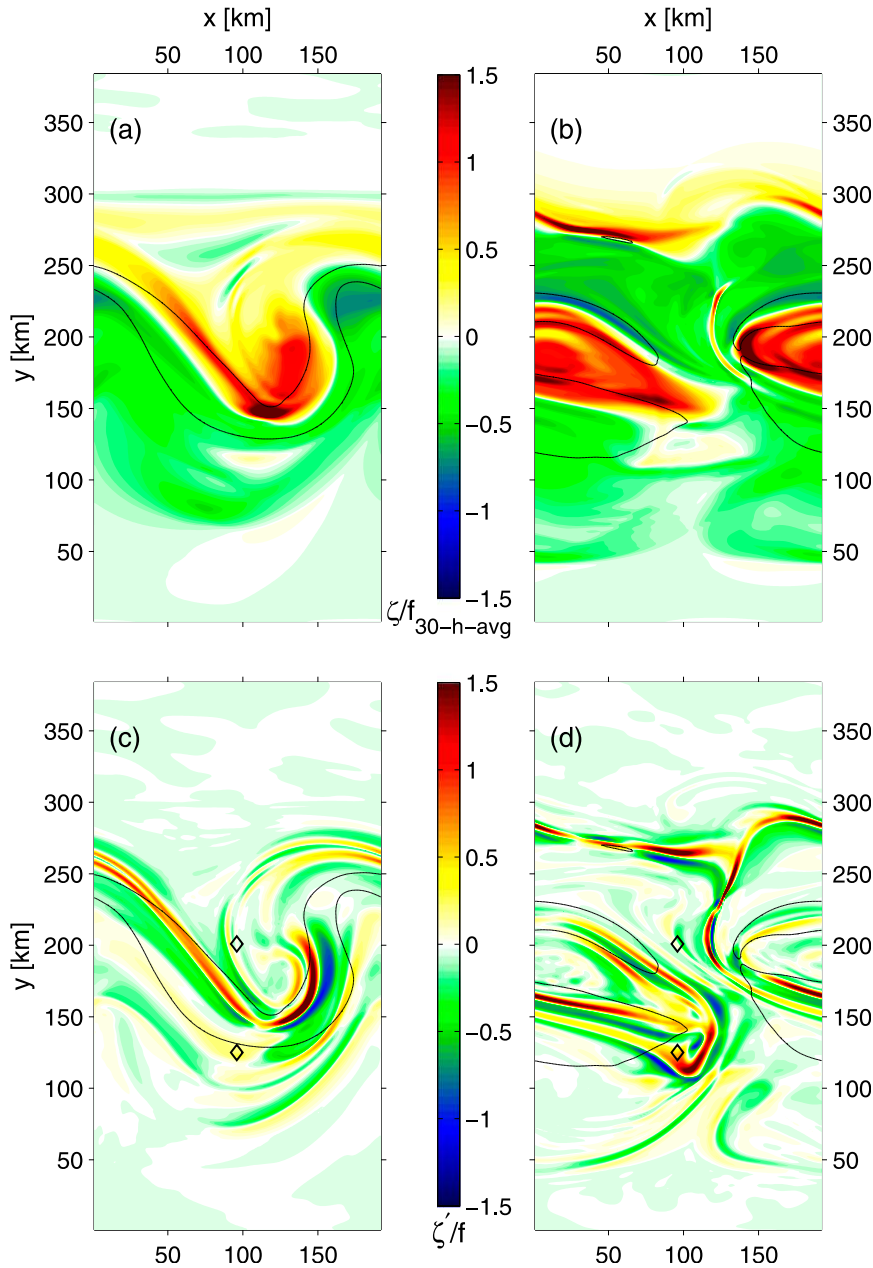
FIG. 5. Plan views of normalized 30-h running average surface vorticity $\overline{\zeta}/f$ for days (a) 6.5 and (b) 10.5 and normalized Eulerian high-pass surface vorticity $\zeta'/f = (\zeta - \overline{\zeta})/f = (v'_x - u'_y)/f$ for days (c) 6.5 and (d) 10.5. Closed black contours indicate the regions where 30-h running averaged surface horizontal velocity magnitude exceeds $1.2 \, \text{m s}^{-1}$. Diamonds in (c) and (d) are Eulerian stations for the time series shown in Figs. 9–10.

isopycnals (Whitt and Thomas 2013) as observed (Fig. 3).

Unlike geostrophic motions, internal waves are associated with horizontal divergence $u_x + v_y$ (Fig. 6; Müller and Siedler 1976; Lien and Müller 1992; Lelong et al. 1999; Plougonven and Snyder 2007; appendix B). High-pass horizontal divergences are strongly intensified

after passage of a meander or eddy during days 10–11 (Figs. 6c,d and 10a). Such wave-intensifying events recur as the front evolves and subinertial confluent regions pass a fixed location (diamonds in Figs. 5c,d; Figs. 9 and 10). Divergence recorded by the particles provides several Lagrangian time series that also exhibit spectral peaks between f and $2f$ (Fig. 7b). Eulerian
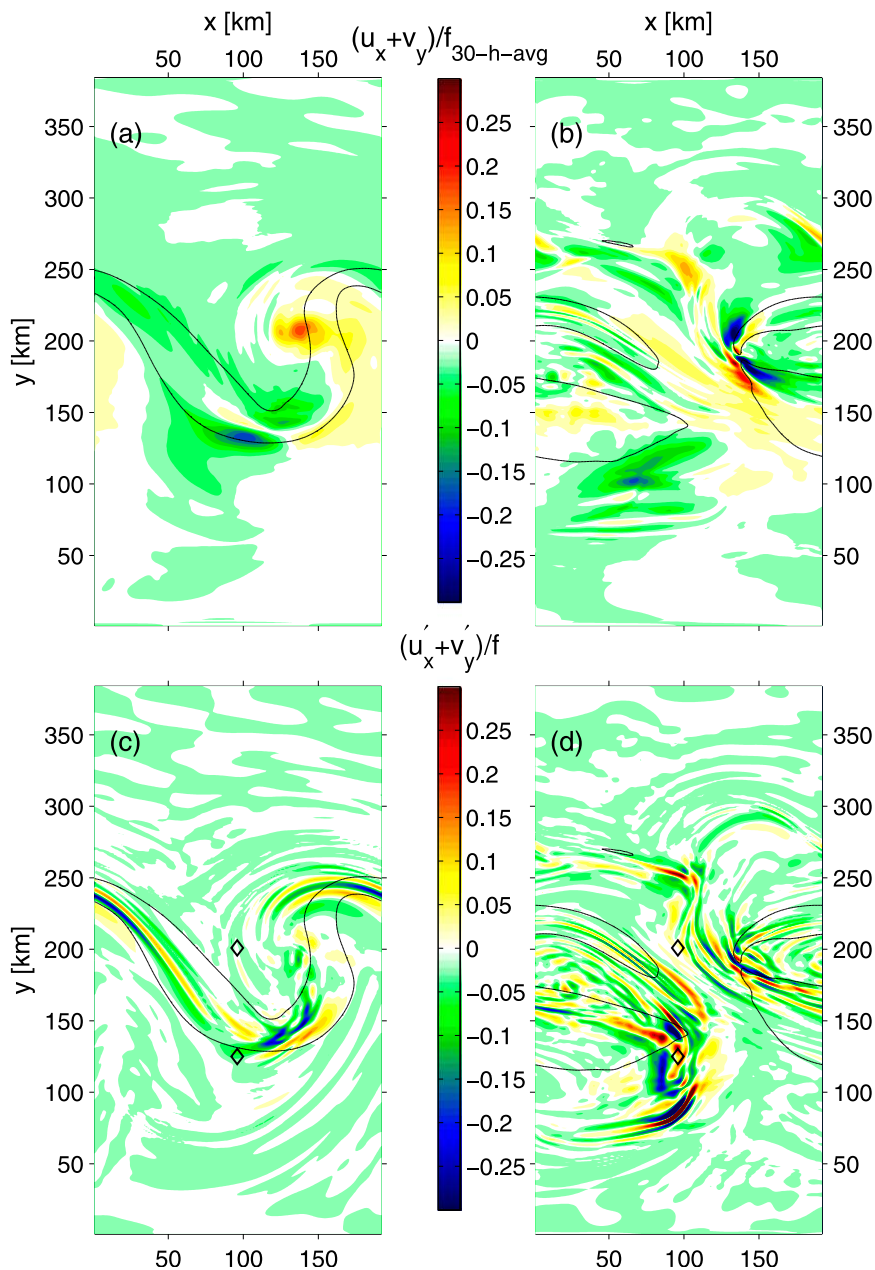
FIG. 6. Plan views at 100-m depth of normalized 30-h running average horizontal divergence $\langle(u_x + v_y)/f\rangle$ for days (a) 6.5 and (b) 10.5 and normalized Eulerian high-pass horizontal divergence $(u'_x + v'_y)/f$ for days (c) 6.5 and (d) 10.5. Closed black contours indicate the regions where 30-h running averaged surface horizontal velocity magnitude exceeds $1.2 \, \mathrm{m \, s^{-1}}$. Diamonds in (c) and (d) are Eulerian stations for the time series shown in Figs. 9–10. The nonzero mean divergence in (a),(b) arises from quasigeostrophic flow and Doppler-shifted near-inertial flow.

divergence spectra (dashed curve in Fig. 7b) show a greater dominance of subinertial variance, indicating that the near-inertial waves' Eulerian frequency is subinertial, like internal lee waves, so these waves might be expected to be confined within the frontal jet

and would not be identified as near inertial in fixed mooring measurements.

For a single propagating near-inertial wave, vertical vorticity $\zeta' = (v'_x - u'_y)/f$ and horizontal divergence $(u'_x + v'_y)/f$ should have similar magnitudes but be 90°
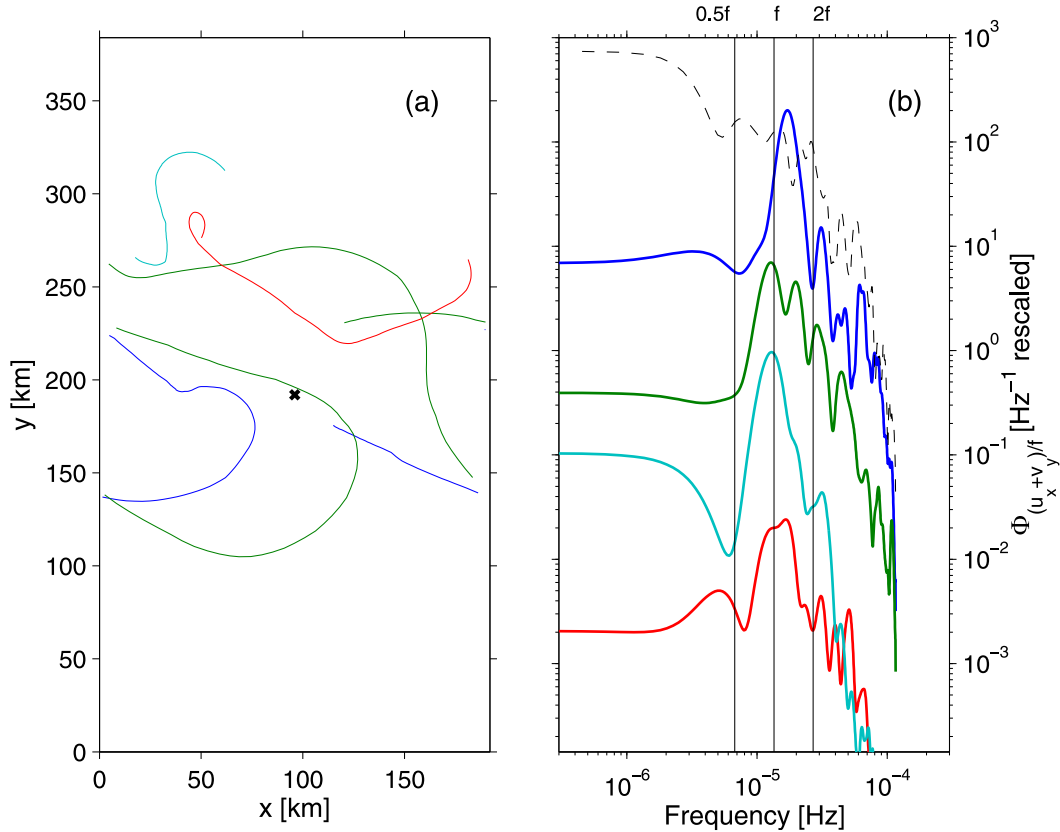
FIG. 7. (a) Trajectories of four sample floats out of 10 000 released in the numerical simulation. (b) Lagrangian frequency spectra of normalized horizontal divergence $(u_x + v_y)/f$ of these four passive floats in the numerical simulation. Instantaneous horizontal divergence is interpolated along the all float trajectories. Four different floats that passed the regions of high confluence were used for the spectra. An Eulerian spectrum at a fixed point ($x = 96$ km, $y = 192$ km), cross in (a), near where these floats passed is shown as a dashed curve. Spectra are computed from the Lagrangian particles shown in Fig. 8. The Eulerian and top Lagrangian spectra are plotted with the correct scales while lower spectra are offset downward by ×[−2.25, −2.5, −3.5] decades, respectively.

out of phase, forming a vector that rotates with time, depth, and horizontal propagation direction. Rotation of the vector composed of high-pass vorticity and divergence is seen in the simulations (Fig. 10), although the relatively larger magnitudes in high-pass vorticity than divergence implies nonnegligible contributions from quasigeostrophic flow in the Eulerian 30-h high-pass velocity. Energy propagation inferred from the rotary properties in the high-pass quantities is downward during days 10–11 to the north of the front (not shown) and upward at 300–400-m depth during days 7–8 to the south of the front (Fig. 10) as was also inferred from the residual vertical shear (Figs. 9c–f). Lagrangian rotary spectra of a vector composed of high-pass horizontal divergence $(u_x' + v_y')$ and relative vorticity $(v_x' - u_y')$, and ratios of horizontal divergence to relative vorticity $(u_x' + v_y')/(v_x' - u_y')$ are also both consistent with the banding being dominated by near-inertial

waves (Figs. 8b and 8c); dominant clockwise rotation of the vector composed of high-pass vorticity and divergence with time in the frequency band f and $2f$ is also found along the Lagrangian particle trajectories (Fig. 8b). Variances of horizontal high-pass divergence $(u_x' + v_y')^2$ and relative vorticity $(v_x' - u_y')^2$ are of the same order of magnitude (Fig. 8c), consistent with near-inertial waves but not geostrophic flow (Kunze 1993).

c. Internal-wave energy fluxes and flux divergences

Near-inertial waves in our unforced model draw their energy from instabilities of the geostrophic flow and may provide a route for transferring energy from low-frequency geostrophic flow to breaking and turbulent dissipation. Using our numerical results, we quantify internal-wave energy E_{IW} conservation following Müller (1976) and Polzin (2010):
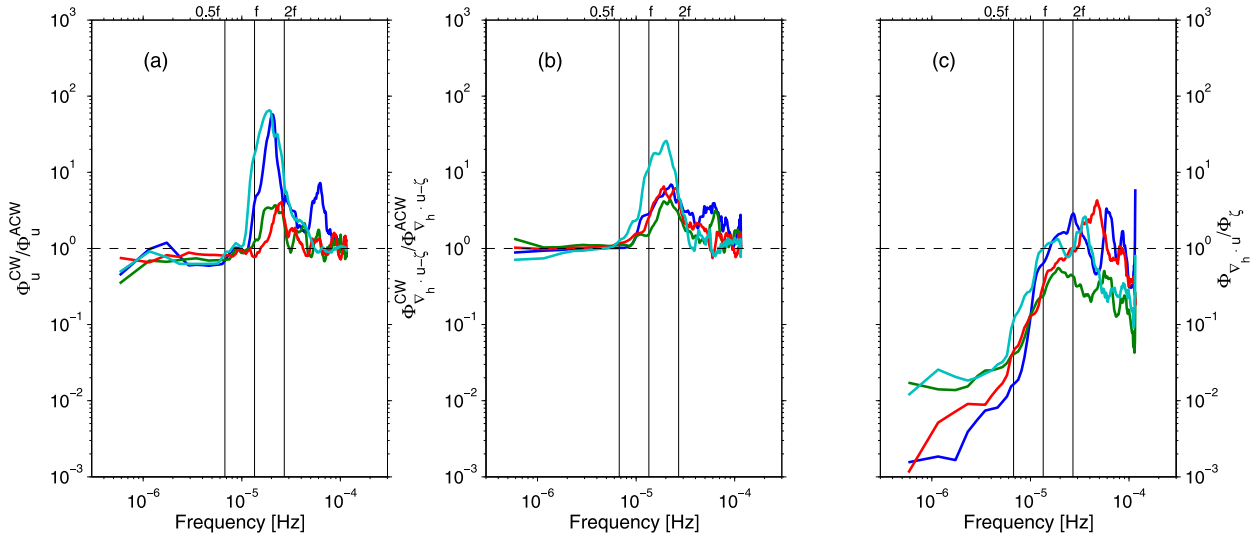
FIG. 8. (a) Lagrangian spectral ratios of clockwise Φ_u^{CW} to anticlockwise Φ_u^{ACW} rotation in time of high-pass velocities u' and v', obtained by four sample passive floats out of 10 000 released in the numerical simulation. (b) Lagrangian spectral ratios of clockwise $\Phi_{\nabla_h u - \zeta}^{\mathrm{CW}}$ to anticlockwise $\Phi_{\nabla_h u - \zeta}^{\mathrm{ACW}}$ rotation for the vector composed of high-pass vorticity $(v'_x - u'_y)$ and divergence $(u'_x + v'_y)$. (c) Lagrangian spectral ratios of high-pass divergence $\Phi_{\nabla_h u}$ to vorticity Φ_ζ. Each estimate of auto- and cospectra have ~ 26 equivalent degrees of freedom with a cosine window, 400 points (20 days every 72 min), and overlapping. High-pass fields are relative to 30-h Eulerian averages. The dashed horizontal lines correspond to ratios of one which are what is expected for continuum $(\omega \gg f)$ internal waves.

$$
\begin{aligned}
\frac{DE_{\mathrm{IW}}}{Dt} + \nabla \cdot \langle p' \mathbf{u}' \rangle = &-\rho_o \left(\langle u'u' \rangle \frac{\partial U}{\partial x} + \langle v'v' \rangle \frac{\partial V}{\partial y} \right) \\
&-\rho_o \left(\langle u'v' \rangle \frac{\partial V}{\partial x} + \langle u'v' \rangle \frac{\partial U}{\partial y} \right) \\
&-\rho_o \left(\langle u'w' \rangle \frac{\partial W}{\partial x} + \langle v'w' \rangle \frac{\partial W}{\partial y} + \langle w'w' \rangle \frac{\partial W}{\partial z} \right) \\
&-\rho_o \left(\langle u'w' \rangle \frac{\partial U}{\partial z} + \langle v'w' \rangle \frac{\partial V}{\partial z} \right) \\
&-\rho_o \left(N^{-2} \langle b'u' \rangle \frac{\partial B}{\partial x} + N^{-2} \langle b'v' \rangle \frac{\partial B}{\partial y} + \langle b'w' \rangle \right) \\
&-\rho_o \left(\langle b'b' \rangle W \frac{\partial N^{-2}}{\partial z} \right) - \varepsilon_{\mathrm{XP}}^{\mathrm{IW}},
\end{aligned} \tag{2}
$$

where DE_{IW}/Dt is the semi-Lagrangian time derivative of internal-wave energy (semi-Lagrangian quantities are obtained with a second set of passive particles that are isobaric so that they only follow the horizontal flow in order to avoid averaging data from different depths with large fluctuations in pressure). In (2), $\nabla \cdot \langle p' \mathbf{u}' \rangle$ is the energy-flux divergence, where $\mathbf{u}'$ and p' are semi-Lagrangian high-pass velocity and pressure relative to low-pass 30-h fifth-order Butterworth fields and $\langle \rangle$ denotes 30-h semi-Lagrangian running averages of the covariance. Uppercase variables are the 30-h semi-Lagrangian running averages for zonal U, meridional V, and vertical W velocities and buoyancy B. The dissipation rate of internal-wave kinetic and potential energy is represented by $\varepsilon_{\mathrm{XP}}^{\mathrm{IW}}$.

Internal-wave energy consists of high-pass kinetic energy $E_{\mathrm{IW}}^K = \rho_o(\langle u'u' \rangle + \langle v'v' \rangle + \langle w'w' \rangle)/2$ and available potential energy $E_{\mathrm{IW}}^P = -g\langle \rho'\rho' \rangle / [2\overline{\rho_z(z)}]$, where $\overline{\rho_z(z)}$ is averaged vertical density gradient as a function of depth alone. Energy transfers into and out of the internal-wave field are evaluated using the left-hand side of (2), with positive values indicating sources (defined as $\int \langle DE_{\mathrm{IW}}/Dt \rangle \, dz + \nabla \cdot \int \langle p'\mathbf{u}' \rangle \, dz > 0$) and negative values sinks (defined as $\int \langle DE_{\mathrm{IW}}/Dt \rangle \, dz + \nabla \cdot \int \langle p'\mathbf{u}' \rangle \, dz < 0$). To obtain the semi-Lagrangian high-pass quantities, 8 million isobaric (fixed depth) passive particles for each simulation case were released in the entire model domain at the outset to record pressure and velocity with reduced Doppler smearing. Because (2)
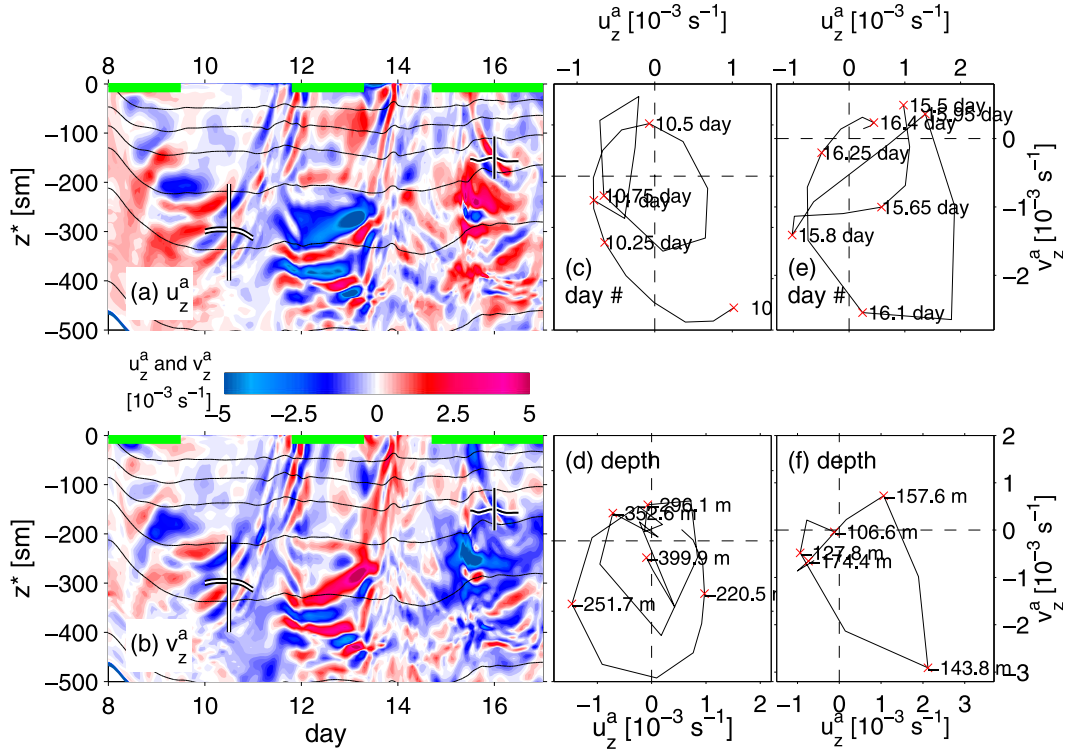
FIG. 9. Depth-time series of WKB-normalized residual (a) zonal shear $u_z^a = u_z + b_y/f$ and (b) meridional shear $v_z^a = v_z - b_x/f$ north of the front (northern diamond in Figs. 5c,d and 6c,d). Depth is WKB-normalized $z^\star = \int N(z)/N_o\, dz$. Temporal hodographs of residual vertical shears u_z^a and v_z^a (c) along the black–white–black horizontal line at the lower left in (a), and (e) along the white–black–white horizontal line at the upper right in (a). Depth hodographs along the (d) black–white–black vertical line and (f) white–black–white vertical line in (a). Green bars along the top axis represent the periods when surface 30-h running averaged horizontal velocity exceeds $0.7\,\mathrm{m\,s^{-1}}$, showing when fronts and intensified near-inertial waves pass this Eulerian location.

includes spatial derivatives, data recorded along particle trajectories are interpolated back onto the model grid after filtering for sub- and superinertial signals. Although particles following only horizontal flows could undergo flow divergence which induces inhomogeneity, the 8 million particles did not exhibit this problem. Also, because Doppler shifting by subinertial vertical flow of $O(10^{-4}–10^{-3})\,\mathrm{m\,s^{-1}} \sim 0.01$–$0.1f$ is smaller than that of horizontal flow 0.1–$1f$, most Doppler shifting is mitigated by the passive isobaric particles.

The internal-wave energy flux is a 30-h semi-Lagrangian temporal running average of the high-pass pressure and velocity covariance $p'\mathbf{u}'$ that is grid averaged on each vertical level with 5-km horizontal resolution. It is readily shown from the geostrophic balance that geostrophic motions do not contribute to energy-flux divergence:

$$\frac{\partial u_g p_g}{\partial x} + \frac{\partial v_g p_g}{\partial y} = \frac{1}{f}\left[-\frac{\partial}{\partial x}\left(\frac{\partial p_g}{\partial y}p_g\right) + \frac{\partial}{\partial y}\left(\frac{\partial p_g}{\partial x}p_g\right)\right]$$
$$= \frac{1}{2f}\left(-\frac{\partial^2 p_g^2}{\partial x \partial y} + \frac{\partial^2 p_g^2}{\partial x \partial y}\right) = 0, \quad (3)$$

where p_g and $\mathbf{u}_g$ are geostrophic reduced pressure and velocity that may be present in the high-pass fields. Furthermore, semi-Lagrangian high-pass velocities are not correlated with high-pass pressure gradients (Figs. 11c and 11d) as was the case for the Eulerian high-pass signals.

To average internal-wave energy flux over a typical 20-km wavelength (Figs. 5 and 6), a 20-km two-dimensional Gaussian horizontal average is applied. The resulting internal-wave energy-flux divergence is not sensitive to small changes in spatial and temporal filtering scales.

Large depth-integrated fluxes $\int \langle p'\mathbf{u}'\rangle\, dz \sim O(1)\,\mathrm{kW\,m^{-1}}$ and flux divergences $\nabla \cdot \int \langle p'\mathbf{u}'\rangle\, dz \sim O(10)\,\mathrm{mW\,m^{-2}}$ occur in the meander trough and crest (Fig. 12). Both zonally averaged { } depth-integrated internal-wave energy sources ($\{\int \langle DE_{\mathrm{IW}}/Dt\rangle\, dz\} + \{\int \langle p'v'\rangle_y\, dz\} > 0$; Fig. 13a) and sinks ($\{\int \langle DE_{\mathrm{IW}}/Dt\rangle\, dz\} + \{\int \langle p'v'\rangle_y\, dz\} < 0$; Fig. 13b), each averaged separately by sign, intensify near the meandering model front as it becomes unstable, becoming statistically stationary near day 6. The strongest generation sites are associated with frontogenesis and
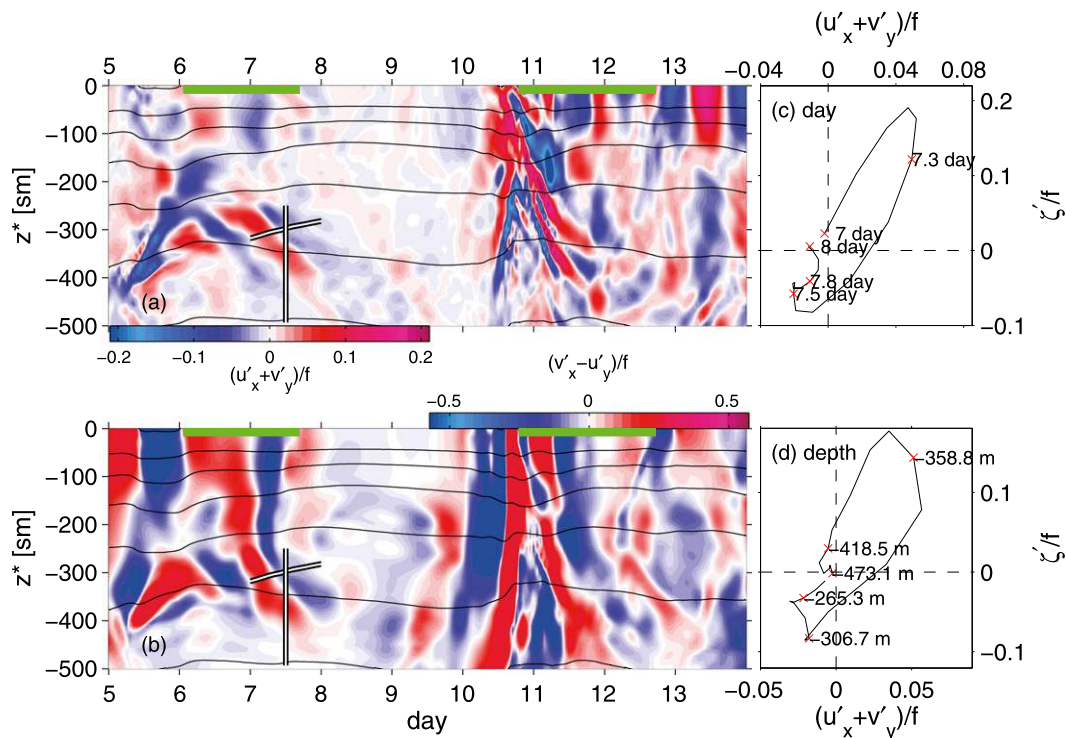
FIG. 10. Depth-time series of normalized fluctuating (a) horizontal divergence $(u'_x + v'_y)/f$ and (b) vorticity $\zeta' = (v'_x - u'_y)/f$ south of the front (southern diamond in Figs. 5c,d and 6c,d). Depth is WKB-normalized $z^\star = \int N(z)/N_o \, dz$. Temporal hodographs of divergence and vorticity along the (c) black–white–black horizontal line in (a). Depth hodographs of divergence and vorticity along the (d) black–white–black vertical line in (a). Green bars on the top abscissa represent the periods when surface 30-h running averaged horizontal velocity exceeds $1.0 \, \mathrm{m \, s^{-1}}$.

frontolysis, consistent with geostrophic adjustment being the source of the waves, as discussed in section 4a.

Local recurrent events of internal-wave generation, or internal-wave power gain $\mathcal{E}_{\mathrm{IW}}$ from the submesoscale subinertial flow, are associated with hotspots of 0.02–$0.05 \, \mathrm{W \, m^{-2}}$ (Fig. 13a). Zonally { } and temporally averaged $\langle \, \rangle$ depth-integrated meridional energy-flux $\{\int \langle p'v' \rangle \, dz\}$ do not radiate far. Maximum fluxes of $O(0.1) \, \mathrm{kW \, m^{-1}}$ within 50 km from the front axis (Fig. 13d) fall to near-zero 100 km from the front. Zonally and temporally averaged, depth-integrated internal-wave energy sources reach $0.02 \, \mathrm{W \, m^{-2}}$, which are largely balanced by sinks within $\pm 100 \, \mathrm{km}$ north and south of the front with sources and sinks appearing to be nearly coincident within the front (Figs. 13a,b,e). This is consistent with Shakespeare and Taylor's (2014) finding that spontaneously generated internal waves are trapped inside a 2D front by frontogenetic confluence as delved into later. Internal-wave energy sinks might be associated with dissipation (Kunze et al. 1995) or reabsorption into the mean since wave energy is not conserved in steady shear flow (Booker and Bretherton 1967; Polzin 2008).

Zonally averaged depth-integrated positive values of the wave–mean flow interaction terms on the right-hand side of (2) show similar time variability and magnitudes to the internal-wave energy source (Figs. 14a and 13a). This is confirmed by the positive correlation coefficient of 0.89 with a near-zero p value between internal-wave energy source and positive interaction terms (Fig. 14b), indicating dynamical consistency. Normal Reynolds-stress deformation terms $-\rho_o(\langle u'u' \rangle \partial U/\partial x + \langle v'v' \rangle \partial V/\partial y)$ dominate over the off-diagonal horizontal shear-stress terms $-\rho_o(\langle u'v' \rangle \partial V/\partial x + \langle u'v' \rangle \partial U/\partial y)$ and by an order of magnitude over other interaction terms. Geostrophic horizontal nondivergence forces $U_x \sim -V_y$ so it is the partial rectilinearity of the near-inertial fluctuations, as discussed in section 3b, that is responsible for the normal Reynolds-stress term being nonzero; model near-inertial rotary signals are not perfectly circular such that $\langle u'u' \rangle - \langle v'v' \rangle$ is $\sim O(10^{-2}) \, \mathrm{m^2 \, s^{-2}}$. This is consistent with internal waves extracting energy from subinertial confluent flows (Müller 1976; Bühler and McIntyre 2005; Polzin 2010; Thomas 2012).

d. Model internal-wave energy sinks and dissipation rates

Similarly, negative values of the right-hand side of (2) agree with the internal-wave energy sinks
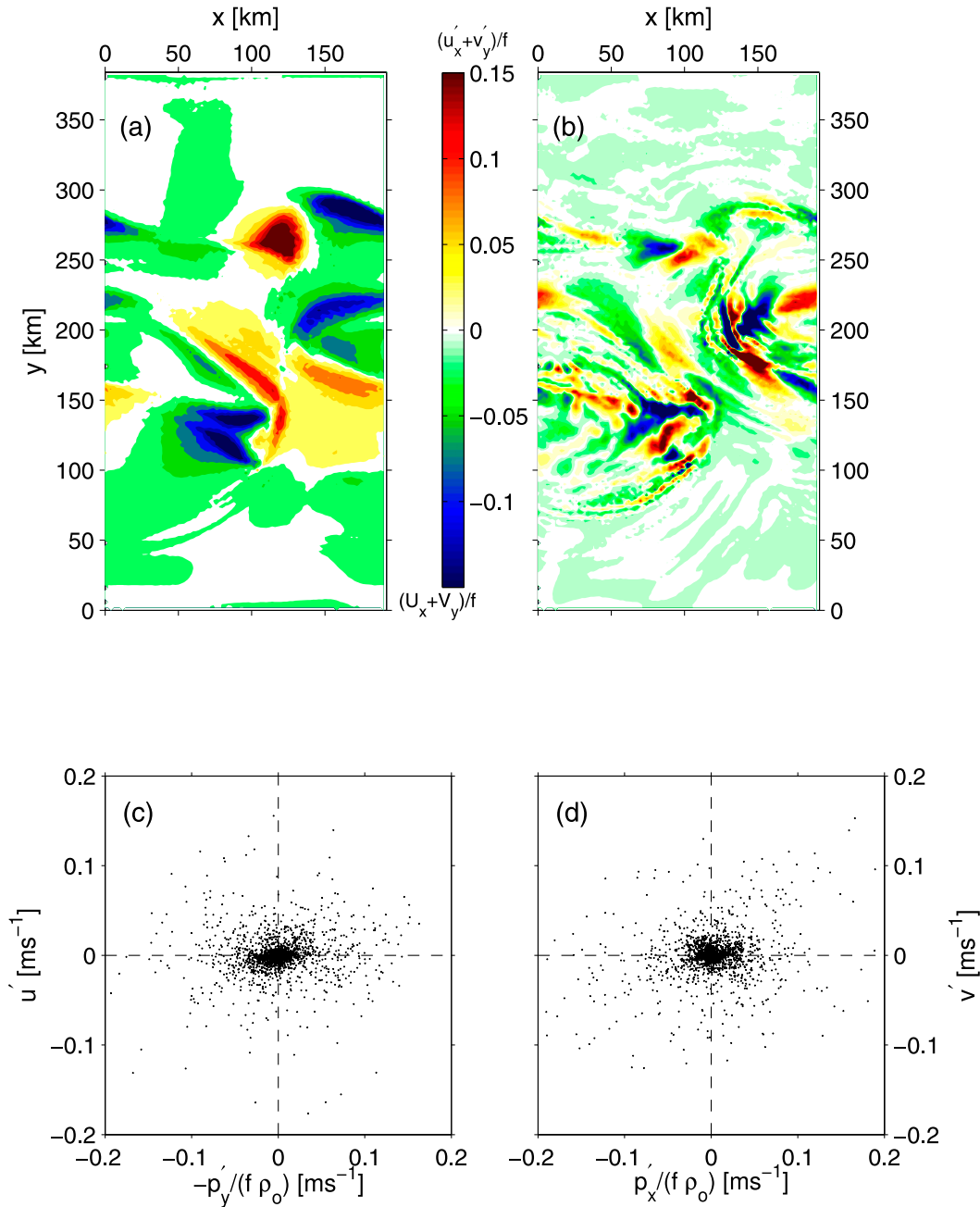
FIG. 11. (a) Top 30-m-averaged semi-Lagrangian 30-h mean $(\overline{u}_x + \overline{v}_y)/f$ and (b) high-pass horizontal divergence $(u'_x + v'_y)/f$ separated using a fifth-order Butterworth low-pass filter with 30-h cutoff period. The semi-Lagrangian mean and high-pass quantities are grid averaged with horizontal resolution of 5 km. Scatterplots for semi-Lagrangian high-pass geostrophic velocities and pressure gradients are shown for the (c) zonal and (d) meridional components. The intense semi-Lagrangian mean divergence shown in (a) arises from quasigeostrophic convergence and divergence of similar order of magnitude to that of the near-inertial wave field (b), consistent with the subinertial convergence and divergence being the sources of spontaneous near-inertial wave generation.

(Figs. 15a and 13b) with the normal-stress terms once more dominating over the off-diagonal horizontal shear-stress terms and by an order of magnitude over other interaction terms. Thus, subinertial

(QG) confluence both emits and absorbs near-inertial waves.

The explicit model kinetic $\mathcal{E}_{xp}^{KE}$ and potential $\mathcal{E}_{xp}^{PE}$ energy dissipation rates can be written
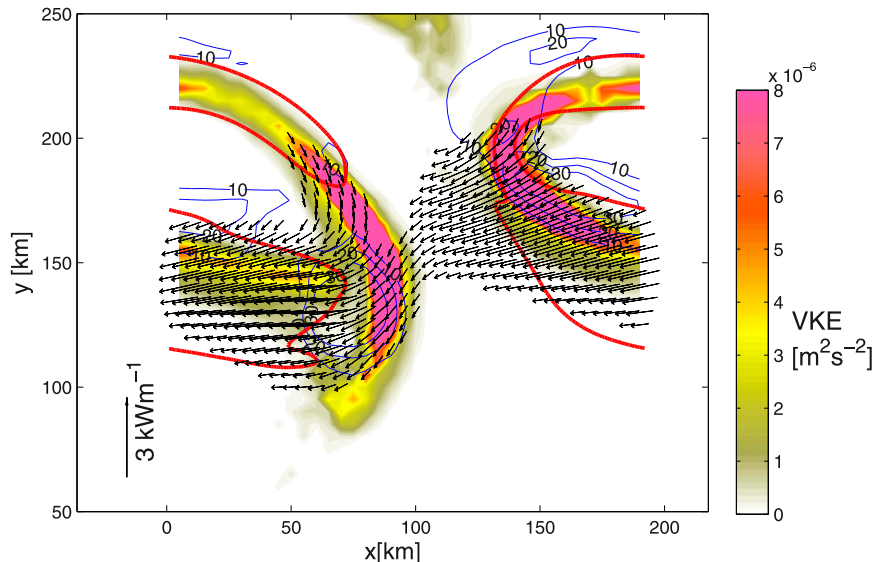
FIG. 12. Snapshot at day 11 from the model showing quasigeostrophic vertical kinetic energy $\mathrm{VKE_{QG}}$ [(8)] in color, evaluated using 30-h semi-Lagrangian running averaged fields (except for frontal depth H_f) with energy fluxes superimposed (black arrows). Arrows are centered on their grid. Energy fluxes less than $0.5\,\mathrm{kW\,m^{-1}}$ are not shown. Blue contours are energy-flux divergence $\nabla \cdot \int \langle p' \mathbf{u}'_h \rangle\, dz > 0\ (\mathrm{mW\,m^{-2}})$. Red contours indicate the regions where 30-h running averaged velocity magnitude exceeds $1.2\,\mathrm{m\,s^{-1}}$.

$$\mathcal{E}_{\mathrm{xp}}^{\mathrm{KE}} = \rho_o \nu_h \left[\left(\frac{\partial \mathbf{u}}{\partial x} \right) \cdot \left(\frac{\partial \mathbf{u}}{\partial x} \right) + \left(\frac{\partial \mathbf{u}}{\partial y} \right) \cdot \left(\frac{\partial \mathbf{u}}{\partial y} \right) \right]$$
$$+ \rho_o \nu_z \left(\frac{\partial \mathbf{u}}{\partial z} \right) \cdot \left(\frac{\partial \mathbf{u}}{\partial z} \right) \quad \text{and} \tag{4}$$

$$\mathcal{E}_{\mathrm{xp}}^{\mathrm{PE}} = -g \frac{\rho K_h |\nabla_h^2 \rho|}{\overline{\rho_z}}, \tag{5}$$

where $\nu_h = K_h = 1\,\mathrm{m^2\,s^{-1}}$ are constant horizontal eddy viscosity and diffusivity, respectively, $\nu_z = 10^{-5}\,\mathrm{m^2\,s^{-1}}$ constant vertical eddy viscosity, and $\overline{\rho_z(z)}$ is the mean density vertical profile. The explicit vertical density diffusion has little impact on the internal-wave potential energy so is omitted from (5). Zonally averaged depth-integrated internal-wave energy dissipation rates, computed using semi-Lagrangian 30-h high-pass quantities (4) and (5), show a weak positive trend with the internal-wave energy sinks, but are an order of magnitude smaller (Fig. 15c). Zonally averaged depth-integrated vertical buoyancy flux $-\rho_o \langle b'w' \rangle$, corresponding to diabatic energy exchange, has similar magnitudes to the high-pass dissipation rate $\sim O(1)\,\mathrm{mW\,m^{-2}}$ (not shown). Zonally averaged depth-integrated total (internal wave and subinertial) energy dissipation rates also show a positive correlation but are still an order of magnitude weaker than internal-wave energy sink (not shown). Downward internal-wave energy flux above the bottom sponge layer is even smaller than integrated energy dissipation (blue curve in Fig. 15c).

These results suggest that, in our numerical simulations, spontaneous internal-wave energy is generated then reabsorbed by the submesoscale subinertial flow (Booker and Bretherton 1967; Polzin 2008, 2010) with only 5–10% dissipating. Both wave energy generation and loss are dominated by normal-stress interaction terms $-\rho_o(\langle u'u' \rangle \partial U/\partial x + \langle v'v' \rangle \partial V/\partial y)$.

e. Summary of modeling results

Motivated by in situ measurements of elevated near-inertial shear and turbulent kinetic energy dissipation in the Kuroshio, numerical experiments were conducted that spontaneously emit internal waves (Fig. 12) from an unforced model Kuroshio Front with properties consistent with near-inertial waves. The simulations find similar banded shear along frontal isopycnals (Figs. 3c and 3d) as the observations (Figs. 3a and 3b). Lagrangian frequencies of these banded features are $(1–2)f$. The estimated average internal-wave power gain within 200 km of the Kuroshio Front is $O(0.01)\,\mathrm{W\,m^{-2}}$ (Fig. 13e) with little energy escaping the front (Fig. 13d). The bulk of the internal-wave energy appears to be reabsorbed within 50–100 km north and south of the source regions (Fig. 13e) with little lost to explicit model dissipation. This implies that most of the subinertial (QG) energy lost to internal waves is redistributed rather than dissipating. Evidence that the model internal-wave energy, energy fluxes, and their divergences and convergences based on
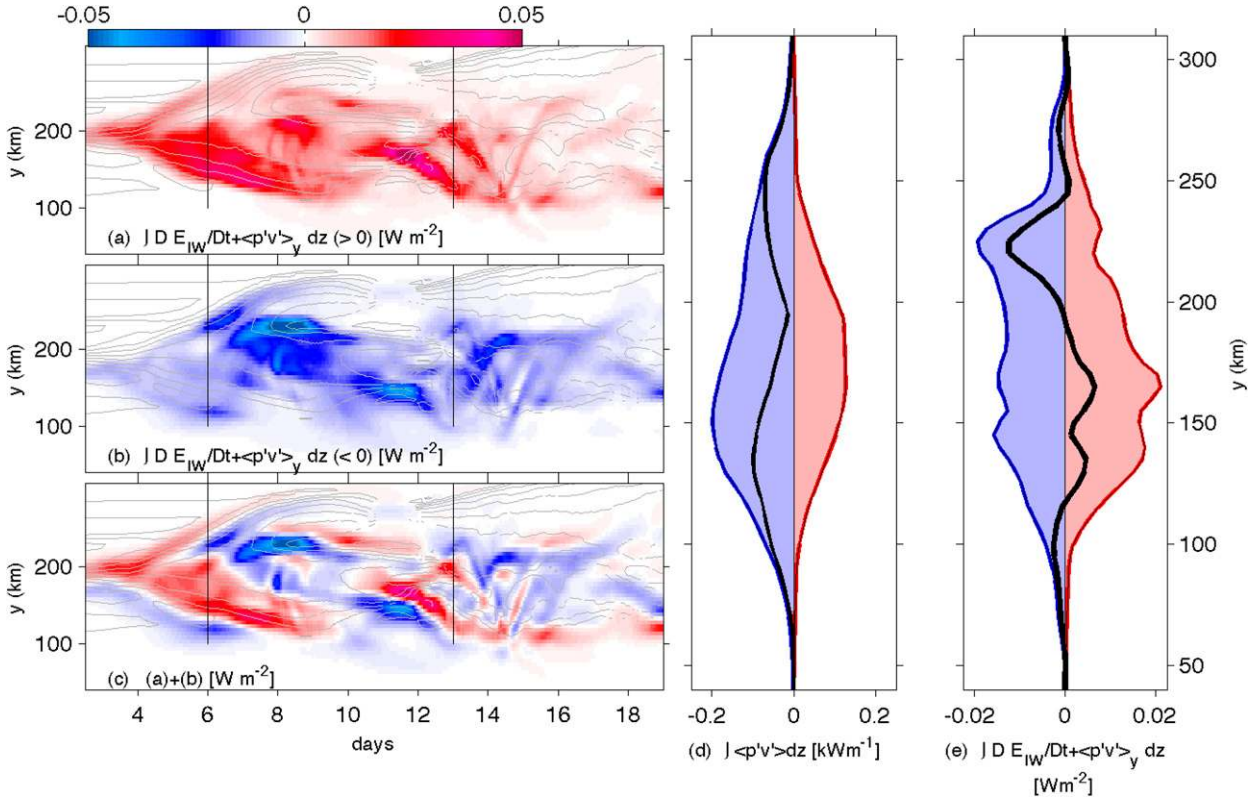
FIG. 13. Time-meridian plots of zonally averaged depth-integrated internal-wave energy (a) source (red), (b) sink (blue), and (c) net difference, (a)+(b), where internal-wave energy sources and sinks have been zonally averaged separately. Gray contours demark surface density. (d) Zonally and temporally averaged depth-integrated northward (red), southward (blue), and net meridional energy fluxes (black). (e) Zonally and temporally averaged depth-integrated internal-wave energy source (red), sink (blue), and net source (black) based on 30-h semi-Lagrangian high-pass quantities.

the high-pass fields are dominated by internal waves comes from (i) the Lagrangian spectra, (ii) the spatial and temporal rotary properties of the residual shears, (iii) absence of correlation between Lagrangian high-pass velocity and pressure gradient, and (iv) that geostrophically balanced flows have no energy-flux convergence associated with them (3).

4. Discussion

The previous laboratory study by Williams et al. (2008) estimated that 1.5 TW could be lost from the wind-driven circulation to spontaneous generation of near-inertial waves globally, while Ferrari and Wunsch (2009) suggested a more modest 0.35 TW based on Polzin's (2010) momentum transfer coefficients, and Thomas (2012) extrapolated 0.1 TW from analytic theory. To quantify the global contribution of gross inertial-wave generation and reabsorption from our simulations, we now estimate the global power transferred to the internal-wave field from the subinertial flow and back again using a two-step process. First, a scaling relation between the internal-wave energy source ($\{\int \langle DE_{\mathrm{IW}}/Dt \rangle \, dz\} + \{\int \langle p'v' \rangle_y \, dz\} > 0$), which we

equate with the internal-wave power gain $\mathcal{E}_{\mathrm{IW}}$, and quasigeostrophic vertical kinetic energy $\mathrm{VKE}_{\mathrm{QG}}$ is derived from the 1-km regional PSOM model. Similarly, a second scaling relationship between internal-wave energy reabsorption rate $\mathcal{E}_{\mathrm{Absp}}$ and $\mathrm{VKE}_{\mathrm{QG}}$ is obtained from the regional PSOM model. These relationships are then applied to the global 0.1°-resolution OGCM for the Earth Simulator (OFES) (Masumoto et al. 2004), which allows estimation of $\mathrm{VKE}_{\mathrm{QG}}$ but not spontaneous generation of near-inertial waves, to obtain global estimates of the internal-wave power gain, reabsorption rates, and the net loss to radiation and dissipation.

a. Scaling for the quasigeostrophic vertical kinetic energy (VKE$_{QG}$)

Horizontal confluence and frontogenesis that arise along meandering fronts create up- and downwelling motions that can be diagnosed using the Eliassen–Sawyer, or quasigeostrophic (QG) ω, equation

$$b_z \frac{\partial^2 \psi}{\partial y_\star^2} + f^2 \frac{\partial^2 \psi}{\partial z^2} = -2 \frac{\partial v^g}{\partial y_\star} \frac{\partial b}{\partial y_\star} \sim \alpha |\nabla_h b| \qquad (6)$$
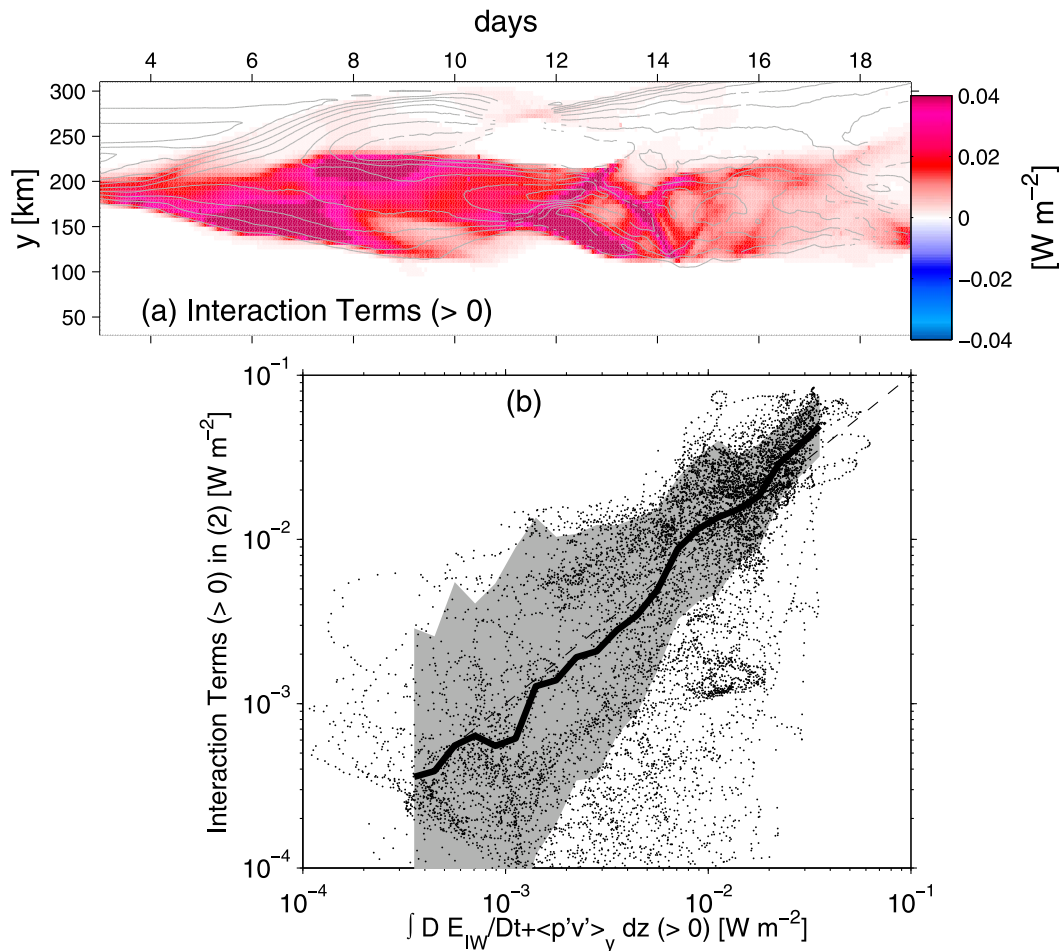
FIG. 14. (a) Time evolution of positive zonally averaged depth-integrated interaction terms on the right-hand side of (2). Gray contours demark surface density. (b) Scatterplot of internal-wave energy source and positive zonally averaged depth-integrated interaction terms. Data exceeding 1.5 standard deviations are excluded from these. The black line represents bin-averaged interaction terms as a function of internal-wave energy source. Gray shading indicates one standard deviation. The bottom sponge layer is excluded in these calculations.

(Hoskins et al. 1978), where ψ is the cross-front streamfunction ($\partial\psi/\partial y_\star = w$, $\partial\psi/\partial z = -v^{\mathrm{ag}}$ with w and v^{ag} as the quasigeostrophic vertical and across-front velocity, respectively), $y_\star$ is the across-front direction, b_z is the buoyancy frequency squared N^2, f is the Coriolis frequency, v^g is the across-frontal geostrophic flow, and $\alpha = \sqrt{(u_x - v_y)^2 + (v_x + u_y)^2}$ is the subinertial horizontal confluence. The first equality on the right-hand side of (6) [i.e., $-2(\partial v^g/\partial y_\star)(\partial b/\partial y_\star)$] is the across-front component of the frontogenetic Q vector (Gill 1982), defined as a product of horizontal buoyancy gradient and confluence, so scales more generally as $\alpha|\nabla_h b|$ as in the second ($\sim$) equality on the right-hand side of (6). The ω equation [(6)] illustrates that quasigeostrophic up- and downwelling $\partial\psi/\partial y_\star$ arise when nondivergent subinertial flow sharpens or weakens isopycnal slopes in fronts. The frontogenetic **Q** vector on the right-hand side of (6) can be interpreted as the forcing due to

this mechanism acting to break geostrophy, while the cross-front secondary circulation ψ arising from this forcing acts to restore geostrophy. Geostrophic adjustment is a well-known mechanism for generation of internal waves (Rossby 1938). Frontogenesis and frontolysis by confluent flows provide the mechanism to force fronts out of balance so they will undergo geostrophic adjustment. Although the vertical velocity, $w = \psi_{y_\star}$ diagnosed from (6) is formally in quasigeostrophic balance, it deforms the buoyancy field and can become unstable, radiating internal waves (Snyder et al. 1993).

Scaling $y_\star$ by the front width L, z by the front depth H, and streamfunction ψ by wL, the QG-ω equation [(6)] implies

$$w \sim \frac{\dfrac{H}{L}\alpha|\nabla_h b|H}{N^2\left(\dfrac{H}{L}\right)^2 + f^2}. \qquad (7)$$
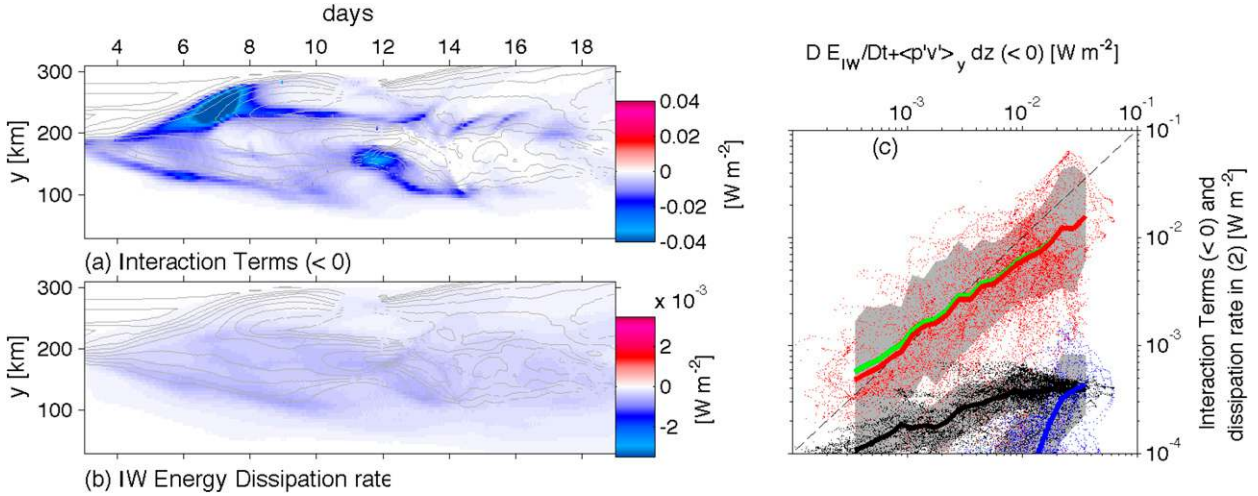
FIG. 15. (a) Time evolution of negative zonally averaged depth-integrated interaction terms on the right-hand side of (2) similar to Fig. 14a. (b) Time evolution of zonally averaged depth-integrated internal-wave energy dissipation rate, the last term of (2). (c) Scatterplot of internal-wave energy sink and negative zonally averaged depth-integrated interaction terms. Data exceeding 1.5 standard deviations are excluded from these. Solid lines represent bin-averaged values as a function of internal-wave energy sink for (red) interaction terms, (black) internal-wave energy dissipation rates, (blue) downward internal-wave energy flux above the bottom sponge layer, and (green) total loss terms on the right-hand side of (2) including downward internal-wave energy flux. Gray shadings are 1 standard deviation. The bottom sponge layer is excluded in these analyses.

Replacing H in the numerator by the vertical integral, H/L by isopycnal slope $s = |\nabla_h b|/N^2$, vertical kinetic energy scales as

$$\text{VKE}_{QG} = \frac{1}{2}w^2 \sim \left(\frac{\langle \overline{s} \rangle \left\langle \int_{-H_b}^{0} \alpha |\nabla_h b| dz \right\rangle}{\langle \overline{N^2} \rangle \langle \overline{s} \rangle^2 + f^2} \right)^2, \qquad (8)$$

where H_b is the bottom depth and $\int_{-H_b}^{0} \alpha |\nabla_h b| \, dz$ is the frontogenetic integral. The overbar represents a depth average over $H_f = \langle \int_{-H_b}^{0} \alpha |\nabla_h b| \, dz/\max(\alpha |\nabla_h b|) \rangle$ and $\langle \ \rangle$ is a temporal average (over a week). The first term in the denominator of (8) is typically smaller than f^2 for large Richardson number $\text{Ri}_g \gg 1$, implying that VKE_{QG} is larger for narrower, stronger fronts driven out of geostrophic balance by stronger confluence.

b. Relation between VKE_{QG} and $\mathcal{E}_{IW}$

Using the 1-km-resolution regional PSOM model, we demonstrate that the energy transfer rate to internal waves $\mathcal{E}_{IW}$ is related to the vertical kinetic energy VKE_{QG} in the cross-frontal circulation that restores balance (Hoskins et al. 1978). By running the regional PSOM model for a range of frontal strengths, a relation between quasigeostrophic vertical kinetic energy VKE_{QG} and internal-wave power gain $\mathcal{E}_{IW}$ is established. To produce a range of isopycnal slopes and frontogenetic integrals, the initial and day-7 buoyancy fields in the original run of

PSOM for 750- and 2000-m-deep run, respectively, are decomposed into mean and deviations as

$$b = \overline{b(x,z)} + cb'(x,y,z), \qquad (9)$$

with $c = 1$ for the original Kuroshio cross section. Here, b is the buoyancy in the model, $\overline{b(x,z)}$ the meridional mean that is a function of alongfront coordinate x and depth z, and $b'(x,y,z)$ the deviation from $\overline{b}$ due to across-front variability in the Kuroshio Front structure. Frontal strength c is varied ($c = 0.25, 0.5$, and 0.75) to produce different initial conditions in thermal-wind balance. The impact of varying frontal strength c and Coriolis frequency f on the dependent variables— isopycnal slope $s = |\nabla_h b|/N^2$ and frontogenetic integral $\int_{-H_b}^{0} \alpha |\nabla_h b| \, dz$—in these PSOM simulations is listed in Table 1; vertical stratification N^2 is nearly constant (3.0– 3.3) $\times 10^{-4}\,\text{s}^{-2}$ (not shown), while isopycnal slope and frontogenetic integral vary by an order of magnitude. VKE_{QG} is not determined directly but inferred from the frontogenetic forcing of the QG ω equation [(6)] using (8). Each term in (8) is first computed by 30-h lowpass-filtered subinertial flow along the semi-Lagrangian iso-baric floats, which is then averaged onto an Eulerian grid before the temporal $\langle \ \rangle$ and vertical averaging in (8). After development of a 100-km-amplitude meander of a few 100-km wavelength around day 6, the rms internal-wave flux divergence is relatively invariant with time. To reduce the spatial gap between peak locations of

TABLE 1. List of parameters governing VKE$_{QG}$, where $\overline{|\mathbf{V}_h b|}/N^2$ is isopycnal slope, $\int_{-H_b}^{0} |\mathbf{V}_h b| \alpha\, dz$ vertically integrated product of α confluence and horizontal buoyancy gradient (frontogenetic integral), and f the Coriolis frequency and model domain depth. The $\overline{|\mathbf{V}_h b|}/N^2$ and $\int_{-H_b}^{0} |\mathbf{V}_h b| \alpha\, dz$ vary depending on frontal strength c in (9) for various initial horizontal buoyancy gradient. Parameters are averaged for PSOM simulations along zonal and meridional direction and temporally for 10 days except f and c. Values in the sponge layers are excluded. The overbar represents average over frontal depth, $H_f = \langle \int_{-H_b}^{0} \alpha |\mathbf{V}_h b|\, dz / \max(\alpha |\mathbf{V}_h b|) \rangle$.

c	$\overline{|\mathbf{V}_h b|}/N^2$	$\int_{-H_b}^{0} |\mathbf{V}_h b| \alpha\, dz$	f	Depth
1.00	0.81×10^{-3}	1.68×10^{-9}	0.83×10^{-4}	750 m
0.75	0.56×10^{-3}	0.84×10^{-9}	0.83×10^{-4}	750 m
0.25	0.15×10^{-3}	0.07×10^{-9}	0.83×10^{-4}	750 m
1.00	1.03×10^{-3}	1.32×10^{-9}	0.83×10^{-4}	2000 m
0.75	0.73×10^{-3}	0.93×10^{-9}	1.40×10^{-4}	2000 m

VKE$_{QG}$ and internal-wave energy-flux divergence evident in Fig. 12, the VKE$_{QG}$, internal-wave power gain $\mathcal{E}_{IW}$, and internal-wave energy reabsorption rate $\mathcal{E}_{Absp}$ are further smoothed over 40 km × 40 km. As the reabsorption rate estimated with all the terms on the right-hand side of (2) has large scatter because of the gradients (Fig. 15), the reabsorption rate is inferred from negative terms on the left-hand side of (2) minus dissipation, $|\int \langle DE_{IW}/Dt \rangle\, dz + \mathbf{V} \cdot \int \langle p'\mathbf{u}' \rangle\, dz < 0| - \int \langle \mathcal{E}_{XP}^{IW} \rangle\, dz$. Averaging more than a week is sufficient to produce an empirical power law for the top 70 percentile of each internal-wave power gain $\mathcal{E}_{IW}$ and VKE$_{QG}$:

$$\mathcal{E}_{IW} = \beta_1 \text{VKE}_{QG}^{\beta_2}, \tag{10}$$

where $\beta_1 = (10^{6.08 \pm 0.01})$ and $\beta_2 = (1.253 \pm 0.003,$ p value $= 0.025)$ (Fig. 16a). The internal-wave energy reabsorption rate $\mathcal{E}_{Absp}$ is also related to VKE$_{QG}$ as

$$\mathcal{E}_{Absp} = \xi_1 \text{VKE}_{QG}^{\xi_2}, \tag{11}$$

where $\xi_1 = (10^{5.837 \pm 0.002})$ and $\xi_2 = (1.217 \pm 0.006, p$ value $= 0.025)$ (Fig. 16b). Results are not significantly altered when model horizontal resolution is refined to 500 m (appendix A), the model depth is extended to 2000 m (appendix B), or when a hydrostatic model is used (appendix C), suggesting that the phenomenon is hydrostatic and well resolved in the 1-km-resolution 750-m-deep PSOM model.

c. Global estimation of internal-wave power gain

We next use the 0.1°-resolution global OFES simulation to estimate VKE$_{QG}$ [(8)] and thence $\mathcal{E}_{IW}$ from
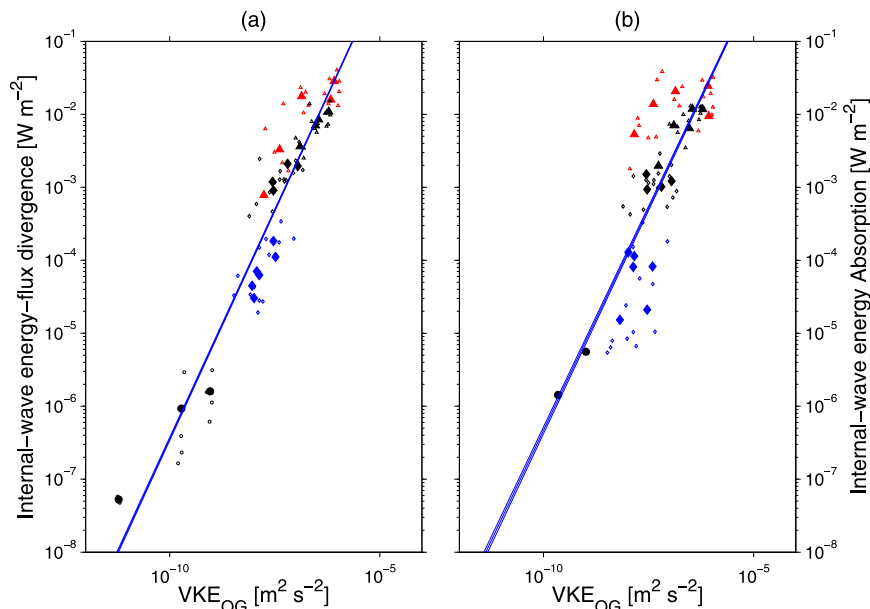

FIG. 16. (a) Top 70 percentile 10-day average internal-wave energy sources (internal-wave power gain $\mathcal{E}_{IW}$) vs top 70 percentile VKE$_{QG}$ in PSOM simulations with differing frontal strengths c and Coriolis frequencies f (Table 1). (b) Top 70 percentile 10-day average internal-wave energy reabsorption rate $\mathcal{E}_{Absp}$ vs top 70 percentile VKE$_{QG}$. Internal-wave energy sources $\mathcal{E}_{IW}$, internal-wave energy reabsorption rates $\mathcal{E}_{Absp} = |\{\int \langle DE_{IW}/Dt \rangle\, dz\} + \{\int \langle p'v' \rangle_y\, dz\} < 0| - \int \mathcal{E}_{XP}^{IW}\, dz$, and VKE$_{QG}$ are averaged over 40 km × 40 km. The blue line indicates least squares power law fits $\mathcal{E}_{IW} = (10^{6.08 \pm 0.01})\text{VKE}_{QG}^{1.253 \pm 0.003}$ with 95% confidence interval in (a) and $\mathcal{E}_{Absp} = (10^{5.8547 \pm 0.002})\text{VKE}_{QG}^{1.217 \pm 0.0006}$ in (b). Black symbols are for the 750-m-deep domain, red symbols 2000-m-deep run, and blue symbols for larger Coriolis frequency 1.4×10^{-4} rad s^{-1} with 2000-m-deep domain. Frontal strengths are indicated by $\triangle$: $c = 1$, $\diamondsuit$: $c = 0.75$, and $\bigcirc$: $c = 0.25$. Large solid marks are zonally averaged values for each case.
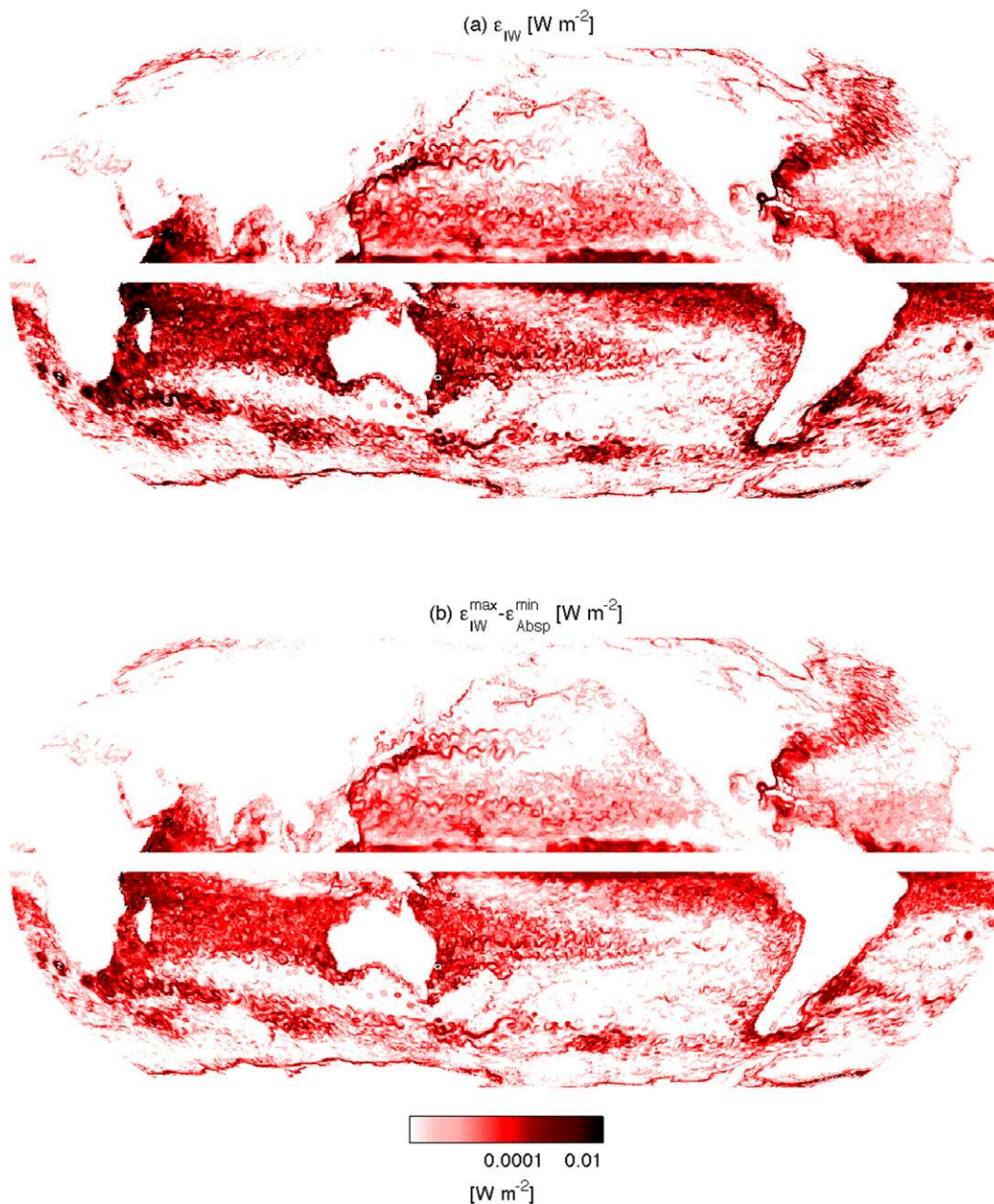
(a) ε_{IW} [W m^{-2}]

(b) $\varepsilon_{IW}^{max} - \varepsilon_{Absp}^{min}$ [W m^{-2}]

0.0001   0.01

[W m^{-2}]

FIG. 17. Global distribution of (a) the gross internal-wave power gain $\mathcal{E}_{IW}$ and (b) the maximum net loss $\mathcal{E}_{IW} - \mathcal{E}_{Absp}$ as inferred from the empirical relations to VKE$_{QG}$ in (10) and (11) evaluated from daily output of the 0.1°-resolution OFES general circulation model and smoothed over 2 weeks and over 0.4° × 0.4°. The maximum net loss is computed from the confidence intervals in (10) and (11). The globally integrated internal-wave power gain $\mathcal{E}_{IW}$ is ~0.36 TW (Table 2) while the net loss is ~0.001–0.047 TW. As with wind power (Wunsch 1998), the equatorial band between ±3° is omitted.

scaling (10) for the World Ocean. VKE$_{QG}$ in the global model is based on arithmetic averages of each term in (8) over a week. To be consistent with the 40-km spatial resolution of VKE$_{QG}$ computed in PSOM, OFES is further smoothed over 0.4° × 0.4°. Quasigeostrophic VKE$_{QG}$ [(8)] is comparable in PSOM and OFES models

when solutions are averaged over a week. In the global model, major ocean frontal systems, including western boundary currents and Antarctic Circumpolar fronts, stand out for their contributions to VKE$_{QG}$ (Fig. 17a). The Indian Ocean also stands out, likely because of the monsoon wind forcing to the north and the Agulhas

TABLE 2. List of the estimated global internal-wave power gain for OFES with lower and upper bound values of $\mathcal{E}_{IW}^{global}$ for 95% confidence interval. The fourth column from the left shows the $\mathcal{E}_{IW}^{global}$ with $\beta_1 = 10^{6.08\pm0.01}$ and $\beta_2 = 1.253 \pm 0.003$ in (10).

| Year | Period | $\mathcal{E}_{IW}^{global}$ 95% confidence level $\mathcal{E}_{IW}^{global} = \beta_1 VKE_{QG}^{\beta_2}$ (TW) | | |
		Lower bound	$\beta_1 = 10^{6.08\pm0.01},$ $\beta_2 = 1.253 \pm 0.003$	Upper bound
1990	1–14 Aug	0.327	0.334	0.341
	15–28 Aug	0.313	0.320	0.327
1991	1–14 Aug	0.332	0.340	0.347
	15–28 Aug	0.364	0.372	0.379
1992	1–14 Aug	0.353	0.361	0.368
	15–28 Aug	0.346	0.353	0.361
1993	1–14 Aug	0.364	0.372	0.379
	15–28 Aug	0.347	0.355	0.362
1994	1–14 Aug	0.362	0.370	0.377
	15–28 Aug	0.348	0.355	0.363
1995	15–28 Aug	0.366	0.375	0.382
1996	1–14 Aug	0.330	0.338	0.345
	15–28 Aug	0.337	0.344	0.351
1997	1–14 Aug	0.380	0.388	0.396
	15–28 Aug	0.348	0.356	0.363
Average	1990–97	0.348	0.356	0.363
Standard deviation	1990–97	0.017	0.018	0.018

retroflection to the south. The globally integrated inferred internal-wave power gain $\mathcal{E}_{IW}^{global}$, excluding a zonal band within $\pm3°$ of the equator, is 0.36 TW (see Table 2) from the quasigeostrophic circulation and eddy field to the internal-wave field. Reabsorption rates $\mathcal{E}_{Absp}$ have similar magnitudes to the internal-wave power gain $\mathcal{E}_{IW}$. With the combined uncertainty in the fits of (10) and (11), it is hard to provide reliable estimates for the
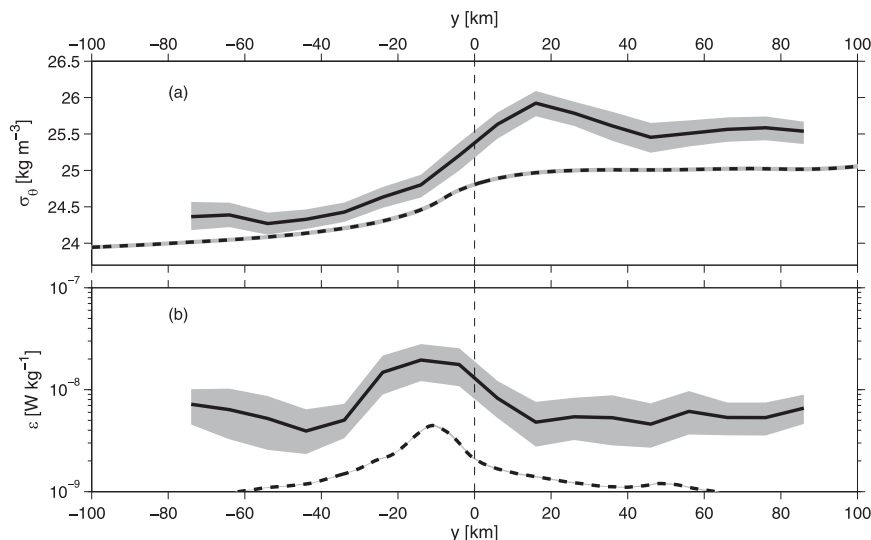

FIG. 18. (a) Upper-300-m-depth-averaged σ_θ as a function of meridional distance y relative to the Kuroshio Front from 2008, 2009, 2011, and 2012 density measurements (solid) and model density (dashed), and (b) 80–250-m-depth-averaged dissipation rates ε as a function of meridional distance y relative to the Kuroshio Front from 2008, 2009, 2011, and 2012 fine- and microstructure measurements (solid) and model inferences of total kinetic energy dissipation rates, $\mathcal{E}_{xp}^{KE}$ (dashed). Shadings for the solid curves are 95% confidence intervals estimated with 300 bootstrap resamplings and for the dashed curves 95% confidence intervals based on normal distribution fits.
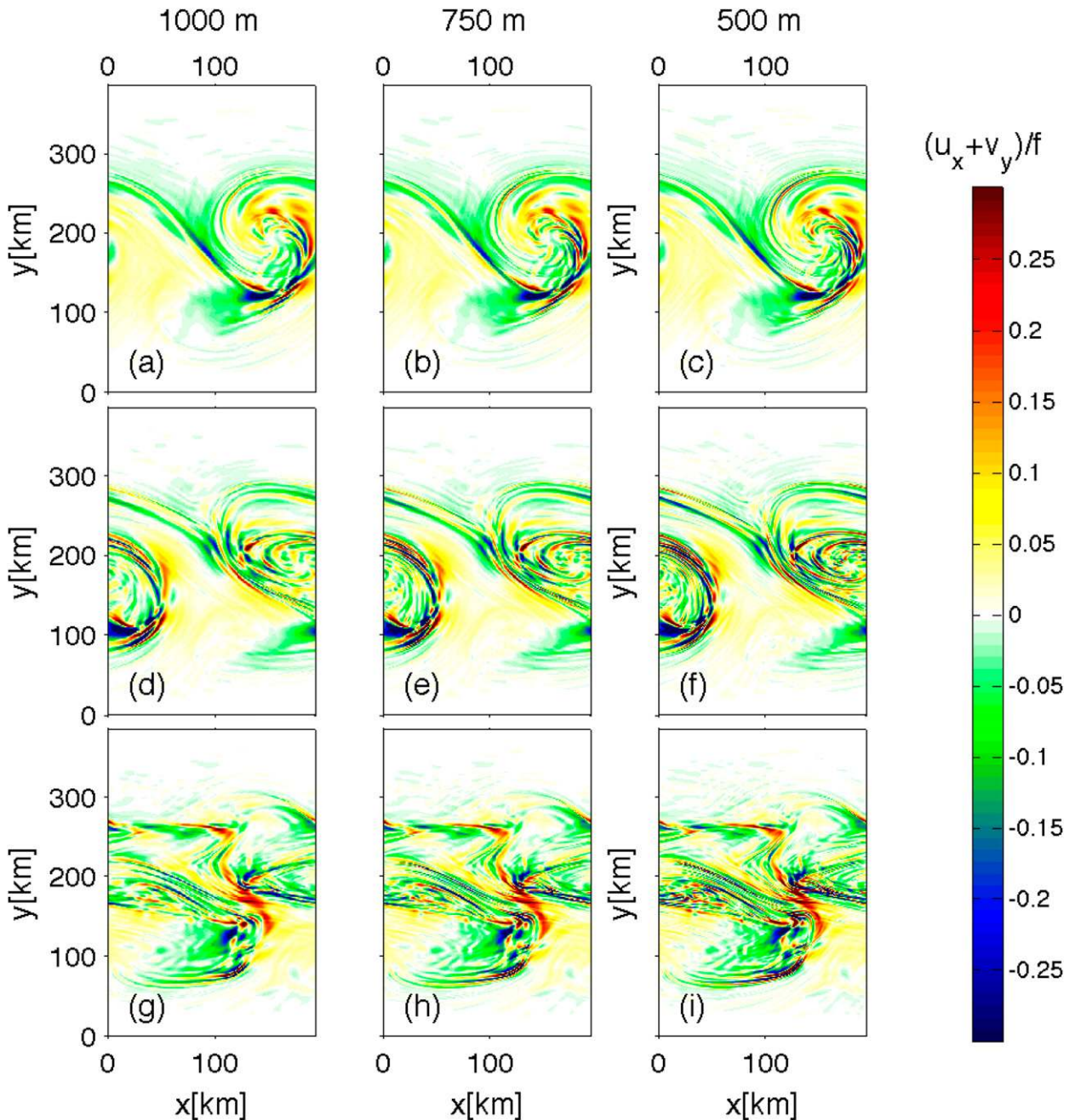
FIG. A1. Comparison of horizontal divergence of the full velocity $(u_x + v_y)/f$ at 100-m depth on days 7.5 (first row), 9.5 (second row), and 11.5 (third row) for horizontal grid resolutions of 1000 m (first column), 750 m (second column), 500 m (third column).

net losses, $\mathcal{E}_{IW} - \mathcal{E}_{Absp}$, but the net loss is 0.001–0.047 TW, no more than $O(15\%)$ of the gross internal-wave power gain $\mathcal{E}_{IW}$ (Fig. 17b), indicating that most of the inertial-wave generation is reabsorbed rather than being dissipated. Thus, these interactions represent a redistribution of subinertial quasigeostrophic energy rather than a significant net loss.

5. Conclusions

Banded shear signals are observed in the Kuroshio Front under calm summer conditions (Fig. 3a). The residual shear has rotary properties in depth and time (Fig. 4), consistent with propagating near-inertial waves. Previous work (Williams et al. 2008; Polzin 2010;
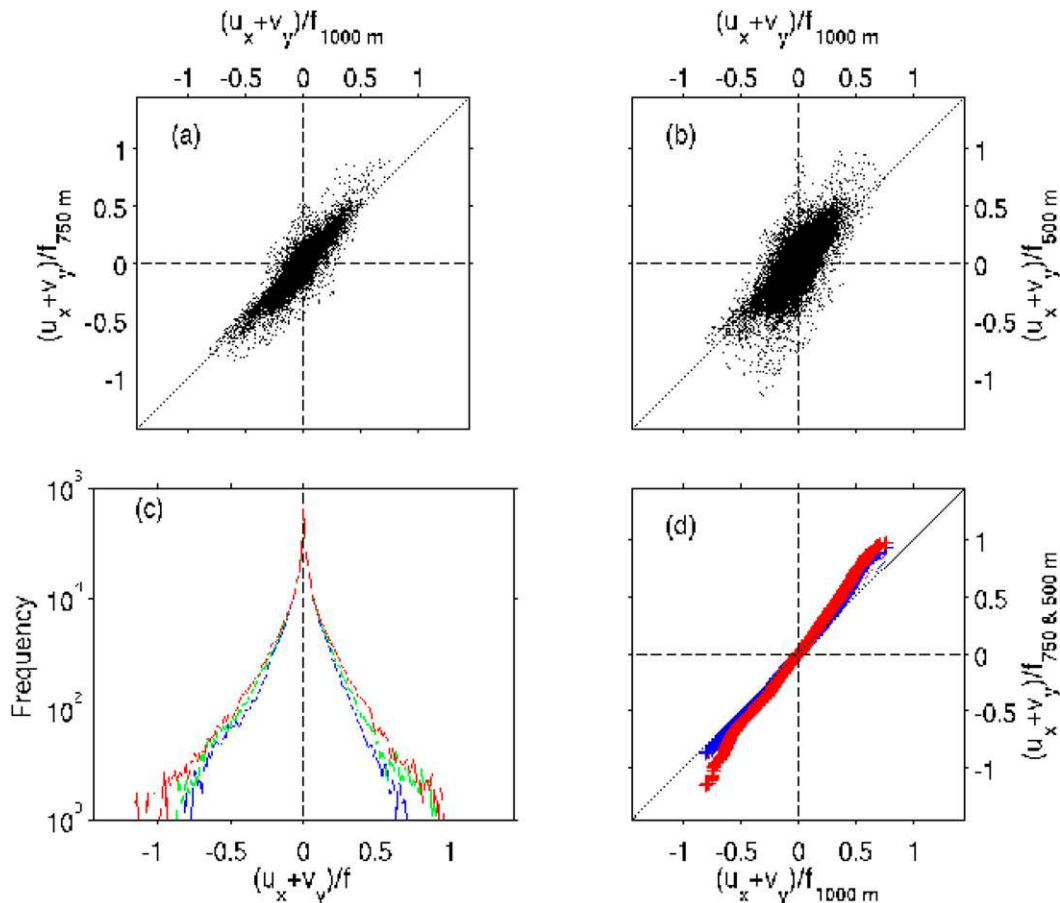
FIG. A2. (a) Scatterplot of normalized horizontal divergence of the full velocity $(u_x + v_y)/f$ at 100-m depth for 1000- and 750-m-resolution model runs using days 7.5, 9.5, and 11.5. The data from coarser-resolution horizontal grids are interpolated onto the 500-m grid. (b) As in (a), but for 1000- and 500-m model resolutions. (c) Histogram of horizontal divergence for (blue) 1000-, (green) 750-, and (red) 500-m resolution. (d) Quantile–quantile plots for horizontal divergence between (blue) 1000- and 750- and (red) 1000- and 500-m resolution.

Thomas 2012) has suggested that frontal instabilities could transfer energy out of the quasigeostrophic flow field into near-inertial waves at rates of 0.1–1.5 TW, suggesting that this mechanism could represent a major sink for the large-scale balanced circulation.

These results motivated numerical simulations of an unforced meandering Kuroshio Front which spontaneously generates large-amplitude near-inertial internal waves associated with frontogenesis/frontolysis. Internal-wave energy is generated at a rate of $O(10)\,\mathrm{mW\,m^{-2}}$, about 10 times higher than estimated in the North Pacific Subtropical Front (Alford et al. 2013). Global estimates of the spontaneous internal-wave generation are 0.36 TW based on a scaling [(10)] between internal-wave power gain $\mathcal{E}_{\mathrm{IW}}$ and quasigeostrophic vertical kinetic energy $\mathrm{VKE}_{\mathrm{QG}}$ (Fig. 16), similar to the global magnitudes inferred by Ferrari and Wunsch (2009) following Sargasso Sea transfer rate estimates by Polzin (2010) and

analytically by Thomas (2012). However, our simulations find that most of the internal-wave power gain is reabsorbed into the subinertial flow so that the net loss from quasigeostrophic energy to model dissipation is no more than 15% of the internal-wave power gain. Thus, compared to other mechanisms such as (i) drag in bottom boundary layers (0.1 TW; Wunsch and Ferrari 2004) and (ii) topographic lee-wave generation (0.2 TW; Nikurashin and Ferrari 2011), spontaneous generation of near-inertial waves (Fig. 1) does not represent a major sink for the large-scale circulation as previously suggested, but only a local redistribution. The gross generation rates are also comparable to low end estimates of 0.2–1.5-TW wind forcing of near-inertial waves (Alford 2001; Furuichi et al. 2008; Plueddemann and Farrar 2006; Rimac et al. 2013), making it a potentially significant, if frontally confined (Fig. 17), source of ocean internal waves.
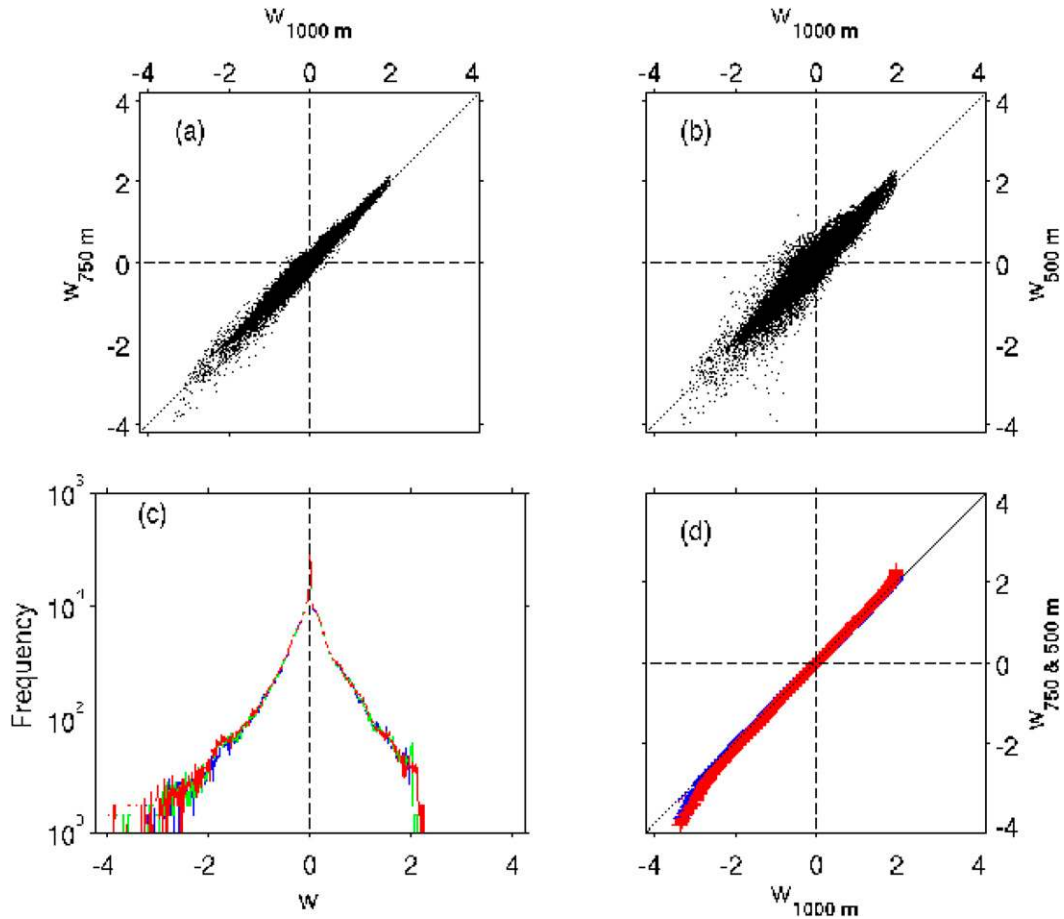
FIG. A3. As in Fig. A2, but for vertical velocity ($10^{-3}\,\mathrm{m\,s^{-1}}$) at 100-m depth.

Directly measured TKE dissipation rates during August 2008, October 2009, August 2011, and August 2012, averaged over 80–250-m depth and within 30 km of the Kuroshio Front, are over $10^{-8}\,\mathrm{W\,kg^{-1}}$, which is an order of magnitude larger than the similarly averaged model subgridscale kinetic energy dissipation rates (Fig. 18). We emphasize that our model is unforced and contains no internal waves at the outset so that all waves originate from the initially geostrophically balanced flow through frontal instability. In the ocean, superposition of frontally generated waves with the background wave field from winds and tides may allow more of the spontaneously generated near-inertial wave energy to be dissipated before it can be reabsorbed as in the numerical model. But wind-forced near-inertial waves may also be trapped and dissipated in fronts so we cannot be certain whether dissipation rates are much larger in the ocean than in the model because of wind-forced or spontaneously generated near-inertial waves.

Scalings from QG vertical kinetic energy $\mathrm{VKE_{QG}}$ [(10)–(11)] provide an empirical parameterization that might be used for global models with sufficient resolution. However, more direct observations and modeling are needed to identify and understand spontaneous generation of the near-inertial internal waves, elucidate how much spontaneously generated wave energy dissipates through wave breaking versus being reabsorbed, and verify that (10) and (11) parameterize these mechanisms in climate models. The question of how the wind-induced large-scale circulation dissipates remains.
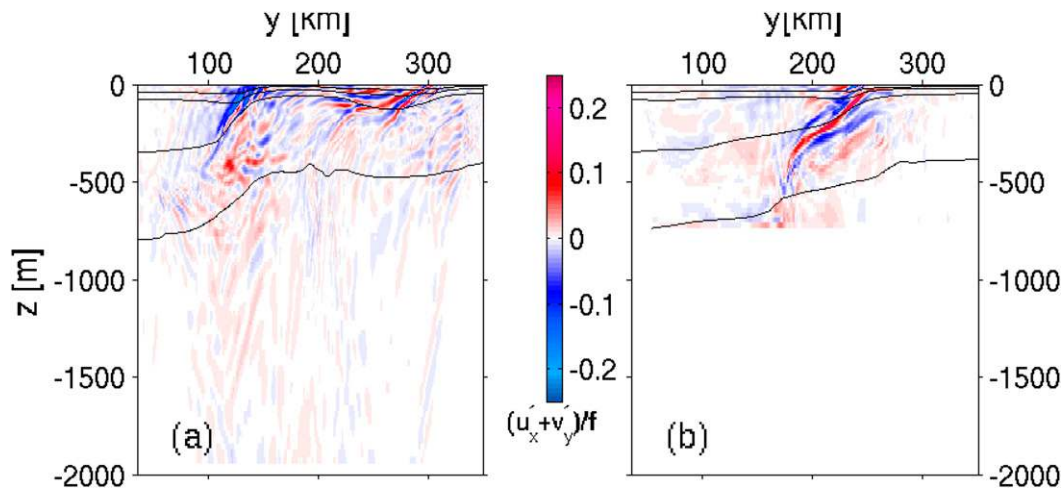
FIG. B1. Comparison of near-inertial horizontal divergence $(u'_x + v'_y)/f$ between the (a) 2000- and (b) 750-m-deep model domains. In the 2000-m domain (a), the downward propagation of the waves below 1000-m depth and their reflections from the bottom are seen. Bottom reflections arise in the 2000-m-deep simulation because the bottom sponge layer has been removed.

APPENDIX A

Sensitivity to Model Resolution

Previous work has shown that model resolution impacts the amplitude and frequency of internal-wave generation in atmospheric fronts (Plougonven and Snyder 2007). Divergences $u_x + v_y$ at 100-m depth differ little between 1000-, 750-, and 500-m-resolution PSOM runs. Near-inertial convergence and divergence is most frequently observed in highly confluent regions of order ~10-km wide, regardless of resolution (Fig. A1).

A histogram shows that divergence approaches $\pm0.8f$ at 1000-m resolution and $\pm f$ at 750- and 500-m resolution (Fig. A2). The extreme values occupy 0.02% and 0.04% of the model domain for 750- and 500-m-resolution runs, respectively. A quantile–quantile plot shows that the difference in the distribution of divergence between 500- and 1000-m-resolution runs only becomes noticeable for divergence magnitudes $|u_x + v_y| > 0.5f$. The Kolmogorov–Smirnov test shows that the null hypothesis of equal distribution between 1000- and 500-m-resolution cases is rejected with 95% confidence intervals (p value: 4.7×10^{-100}) because of large extreme values at 500-m resolution (Fig. A2).

The vertical velocity at 100-m depth shows more similarity among the three resolutions (Fig. A3), although the same null hypothesis is rejected (p value: 9.3×10^{-31}) because w is skewed toward stronger downwelling (Mahadevan and Tandon 2006) in the 500-m-resolution run (Fig. A3). Stronger downwelling is associated with superinertial w' mostly by internal

waves in highly stratified simulations initialized with summer observation data. Here, 8.2% (1.6%) of the data points differ in flow divergence $u_x + v_y$ (vertical velocity w) between 1000- and 500-m resolution by more than one standard deviation. Compared to the 1000-m run, the magnitude of the power gain increases by as much as 6% and 11% at 750- and 500-m runs. However, the timing and locations of the sources and sinks are indistinguishable among different resolutions. These results suggest that our 1-km model resolution is sufficient to simulate near-inertial wave generation by the unstable Kuroshio Front, though it may underestimate the power transfer from balanced flow to internal waves by up to 10%.

APPENDIX B

Sensitivity to Depth of the Model Domain

Our PSOM model domain is limited to 750 m vertically. The real Kuroshio region has a depth of about 4000 m. The depth of the domain may alter baroclinic instability and associated confluence fields, which are important for wave generation. Although the mesoscale meander takes several weeks longer to develop in a 2000-m-deep domain than the 750-m domain, the 2000-m simulations exhibit similar banded structures in horizontal divergence, signifying generation of internal waves (Fig. B1). Downward propagation of the waves below 1000-m depth and their reflection from the bottom are seen, because the bottom sponge layer is removed for simulations with 2000-m model depth. The

results from the 2000-m-depth model scale identically to the 750-m domain for the internal-wave power gain [(6)], suggesting that the scaling law can be applied regardless of domain depth (Fig. 16) and results from the global OFES model are still valid.

APPENDIX C

Hydrostatic versus Nonhydrostatic

We also ran the hydrostatic primitive equation ROMS model (Shchepetkin and McWilliams 2005) to examine internal-wave generation by meandering fronts. This model was initialized with the same August 2008 density section (section 3a). The model's horizontal resolution is ~1000 m and uses 100 vertical levels. No explicit diffusion is included. Banding in horizontal divergence emerges at the meander trough and crest with similar magnitude and wavelengths as the PSOM simulations, suggesting that inertial-wave generation is hydrostatic.

REFERENCES

Alford, M. H., 2001: Internal swell generation: The spatial distribution of energy flux from the wind to mixed layer near-inertial motions. *J. Phys. Oceanogr.,* **31,** 2359–2368, doi:10.1175/1520-0485(2001)031<2359:ISGTSD>2.0.CO;2.

——, A. Y. Shcherbina, and M. C. Gregg, 2013: Observations of near-inertial gravity waves radiating from a frontal jet. *J. Phys. Oceanogr.,* **43,** 1225–1239, doi:10.1175/JPO-D-12-0146.1.

Booker, J. R., and F. P. Bretherton, 1967: The critical layer for internal gravity waves in a shear flow. *J. Fluid Mech.,* **27,** 513–529, doi:10.1017/S0022112067000515.

Bühler, O., and M. McIntyre, 2005: Wave capture and wave-vortex duality. *J. Fluid Mech.,* **534,** 67–95, doi:10.1017/S0022112005004374.

Danioux, E., J. Vanneste, P. Klein, and H. Sasaki, 2012: Spontaneous inertia-gravity-wave generation by surface-intensified turbulence. *J. Fluid Mech.,* **699,** 153–173, doi:10.1017/jfm.2012.90.

Doubell, M. J., H. Yamazaki, H. Li, and Y. Kokubu, 2009: An advanced laser-based fluorescence microstructure profiler (TurboMAP-L) for measuring bio-physical coupling in aquatic systems. *J. Plankton Res.,* **31,** 1441–1452, doi:10.1093/plankt/fbp092.

Ferrari, R., and C. Wunsch, 2009: Ocean circulation kinetic energy: Reservoirs, sources, and sinks. *Annu. Rev. Fluid Mech.,* **41,** 253–282, doi:10.1146/annurev.fluid.40.111406.102139.

Fofonoff, N. P., 1981: The Gulf Stream system. *Evolution of Physical Oceanography: Scientific Surveys in Honor of Henry Stommel,* B. A. Warren and C. Wunsch, Eds., The MIT Press, 112–139.

Ford, R., 1994: Gravity wave radiation from vortex trains in rotating shallow water. *J. Fluid Mech.,* **281,** 81–118, doi:10.1017/S0022112094003046.

Furuichi, N., T. Hibiya, and Y. Niwa, 2008: Model-predicted distribution of wind-induced internal-wave energy in the world's oceans. *J. Geophys. Res.,* **113,** C09034, doi:10.1029/2008JC004768.

Gill, A. E., 1982: *Atmosphere-Ocean Dynamics.* International Geophysics Series, Vol. 30, Academic Press, 662 pp.

Hoskins, B. J., I. Draghici, and H. C. Davies, 1978: A new look at the ω-equation. *Quart. J. Roy. Meteor. Soc.,* **104,** 31–38, doi:10.1002/qj.49710443903.

Inoue, R., M. C. Gregg, and R. R. Harcourt, 2010: Mixing rates across the Gulf Stream, Part 1: On the formation of Eighteen Degree Water. *J. Mar. Res.,* **68,** 643–671, doi:10.1357/002224011795977662.

Kouketsu, S., I. Yasuda, and Y. Hiroe, 2007: Three-dimensional structure of frontal waves and associated salinity minimum formation along the Kuroshio Extension. *J. Phys. Oceanogr.,* **37,** 644–656, doi:10.1175/JPO3026.1.

Kunze, E., 1985: Near-inertial wave propagation in geostrophic shear. *J. Phys. Oceanogr.,* **15,** 544–565, doi:10.1175/1520-0485(1985)015<0544:NIWPIG>2.0.CO;2.

——, 1993: Submesoscale dynamics near a seamount. Part II: The partition of energy between internal waves and geostrophy. *J. Phys. Oceanogr.,* **23,** 2589–2601, doi:10.1175/1520-0485(1993)023<2589:SDNASP>2.0.CO;2.

——, R. W. Schmitt, and J. M. Toole, 1995: The energy balance in a warm-core ring's near-inertial critical layer. *J. Phys. Oceanogr.,* **25,** 942–957, doi:10.1175/1520-0485(1995)025<0942:TEBIAW>2.0.CO;2.

Lelong, M.-P., T. Dunkerton, and D. Darr, 1999: Near-inertial wave generation on an unsteady ocean current. *Dynamics of Oceanic Internal Gravity Waves II: Proc. 'Aha Huliko'a Hawaiian Winter Workshop,* Honolulu, HI, University of Hawai'i at Mānoa, 197–203. [Available online at http://www.soest.hawaii.edu/PubServices/1999pdfs/Lelong.pdf.]

Lien, R.-C., and P. Müller, 1992: Normal-mode decomposition of small-scale oceanic motions. *J. Phys. Oceanogr.,* **22,** 1583–1592, doi:10.1175/1520-0485(1992)022<1583:NMDOSS>2.0.CO;2.

Mahadevan, A., and A. Tandon, 2006: An analysis of mechanisms for submesoscale vertical motion at ocean fronts. *Ocean Modell.,* **14,** 241–256, doi:10.1016/j.ocemod.2006.05.006.

——, J. Oliger, and R. Street, 1996a: A nonhydrostatic mesoscale ocean model. Part I: Well-posedness and scaling. *J. Phys Oceanogr.,* **26,** 1868–1880, doi:10.1175/1520-0485(1996)026<1868:ANMOMP>2.0.CO;2.

——, ——, and ——, 1996b: A nonhydrostatic mesoscale ocean model. Part II: Numerical implementation. *J. Phys Oceanogr.,* **26,** 1881–1900, doi:10.1175/1520-0485(1996)026<1881:ANMOMP>2.0.CO;2.

Masumoto, Y., and Coauthors, 2004: A fifty-year eddy-resolving simulation of the world ocean—Preliminary outcomes of OFES (OGCM for the Earth Simulator). *J. Earth Simul.,* **1,** 35–56.

Mooers, C. N., 1975: Several effects of baroclinic current on the cross-stream propagation of inertial-internal waves. *Geophys. Fluid Dyn.,* **6,** 245–275, doi:10.1080/03091927509365797.

Müller, P., 1976: On the diffusion of momentum and mass by internal gravity waves. *J. Fluid Mech.,* **77,** 789–823, doi:10.1017/S0022112076002899.

——, and G. Siedler, 1976: Consistency relations for internal wave. *Deep-Sea Res.,* **23,** 613–628.

Nagai, T., A. Tandon, H. Yamazaki, and M. J. Doubell, 2009: Evidence of enhanced turbulent dissipation in the frontogenetic Kuroshio Front thermocline. *Geophys. Res. Lett.,* **36,** L12609, doi:10.1029/2009GL038832.

——, ——, ——, ——, and S. Gallager, 2012: Direct observations of microscale turbulence and thermohaline structure in the Kuroshio Front. *J. Geophys. Res.,* **117,** C08013, doi:10.1029/2011JC007228.

Nasmyth, P. W., 1970: Oceanic turbulence. Ph.D. thesis, University of British Columbia, 69 pp. [Available online at https://circle.ubc.ca/handle/2429/34947.]

Nikurashin, M., and R. Ferrari, 2011: Global energy conversion rate from geostrophic flows into internal lee waves in the deep ocean. *Geophys. Res. Lett.,* **38,** L08610, doi:10.1029/2011GL046576.

Oort, A. H., L. A. Anderson, and J. P. Peixoto, 1994: Estimates of the energy cycle of the oceans. *J. Geophys. Res.,* **99,** 7665–7688, doi:10.1029/93JC03556.

Plougonven, R., and C. Snyder, 2007: Inertia–gravity waves spontaneously generated by jets and fronts. Part I: Different baroclinic life cycles. *J. Atmos. Sci.,* **64,** 2502–2520, doi:10.1175/JAS3953.1.

Plueddemann, A. J., and J. T. Farrar, 2006: Observations and models of the energy-flux from the wind to mixed-layer inertial currents. *Deep-Sea Res. II,* **53,** 5–30, doi:10.1016/j.dsr2.2005.10.017.

Pollard, R. T., and R. C. Millard, 1970: Comparison between observed and simulated wind-generated inertial oscillations. *Deep-Sea Res.,* **17,** 813–821.

Polzin, K. L., 2008: Mesoscale eddy-internal wave coupling. Part I: Symmetry, wave capture, and results from the Mid-Ocean Dynamics Experiment. *J. Phys. Oceanogr.,* **38,** 2556–2574, doi:10.1175/2008JPO3666.1.

——, 2010: Mesoscale eddy-internal wave coupling. Part II: Energetics and results from PolyMode. *J. Phys. Oceanogr.,* **40,** 789–801, doi:10.1175/2009JPO4039.1.

Rainville, L., and R. Pinkel, 2004: Observations of energetic high-wavenumber internal waves in the Kuroshio. *J. Phys. Oceanogr.,* **34,** 1495–1505, doi:10.1175/1520-0485(2004)034<1495:OOEHIW>2.0.CO;2.

Rimac, A., J. S. von Storch, C. Eden, and H. Haak, 2013: The influence of high-resolution wind-stress field on the power input to near-inertial motions in the ocean. *Geophys. Res. Lett.,* **40,** 4882–4886, doi:10.1002/grl.50929.

Rossby, C. G., 1938: On the mutual adjustment of pressure and velocity distributions in certain simple current system, II. *J. Mar. Res.,* **1,** 239–263.

Saito, K., and Coauthors, 2006: The operational JMA non-hydrostatic mesoscale model. *Mon. Wea. Rev.,* **134,** 1266–1298, doi:10.1175/MWR3120.1.

Shakespeare, C. J., and J. R. Taylor, 2014: The spontaneous generation of inertia-gravity waves during frontogenesis forced by large strain: Theory. *J. Fluid Mech.,* **757,** 817–853, doi:10.1017/jfm.2014.514.

Shchepetkin, A. F., and J. C. McWilliams, 2005: A split-explicit, free-surface, topography following coordinates ocean model. *Ocean Modell.,* **9,** 347–404, doi:10.1016/j.ocemod.2004.08.002.

Snyder, C., W. C. Skamarock, and R. Rotunno, 1993: Frontal dynamics near and following frontal collapse. *J. Atmos. Sci.,* **50,** 3194–3211, doi:10.1175/1520-0469(1993)050<3194:FDNAFF>2.0.CO;2.

Thomas, L. N., 2012: On the effects of frontogenetic strain on symmetric instability and inertia-gravity waves. *J. Fluid Mech.,* **711,** 620–640, doi:10.1017/jfm.2012.416.

Whitt, D., and L. Thomas, 2013: Near inertial waves in strongly baroclinic currents. *J. Phys. Oceanogr.,* **43,** 706–725, doi:10.1175/JPO-D-12-0132.1.

Williams, P. D., T. W. N. Haine, and P. L. Read, 2008: Inertia–gravity waves emitted from balanced flow: Observations, properties, and consequences. *J. Atmos. Sci.,* **65,** 3543–3556, doi:10.1175/2008JAS2480.1.

Winkel, D. P., M. C. Gregg, and T. B. Sanford, 2002: Patterns of shear and turbulence across the Florida current. *J. Phys. Oceanogr.,* **32,** 3269–3285, doi:10.1175/1520-0485(2002)032<3269:POSATA>2.0.CO;2.

Wunsch, C., 1998: The work done by the wind on the oceanic general circulation. *J. Phys. Oceanogr.,* **28,** 2332–2340, doi:10.1175/1520-0485(1998)028<2332:TWDBTW>2.0.CO;2.

——, and R. Ferrari, 2004: Vertical mixing, energy, and the general circulation of the oceans. *Annu. Rev. Fluid Mech.,* **36,** 281–314, doi:10.1146/annurev.fluid.36.050802.122121.